Journal of Colloid and Interface Science 691 (2025) 137454

Contents lists available at ScienceDirect

Journal of Colloid And Interface Science

journal homepage: www.elsevier.com/locate/jcis

Regular Article

# The potential of metal–organic framework MIL-101(Al)–$NH_2$ in the forefront of antiviral protection of cells *via* interaction with SARS-CoV-2 spike RBD protein and their antibacterial action mediated with hypericin and photodynamic treatment

Veronika Huntošová [a,b,*], Anass Benziane [c], Luboš Zauška [d,e], Luboš Ambro [a], Soňa Olejárová [a,f], Jaroslava Joniová [g], Nina Hlávková [d], Georges Wagnières [g], Gabriela Zelenková [h], Pavel Diko [i], Jozef Bednarčík [j], Florina Zákány [c], Tamás Kovács [c], Erik Sedlák [a,k], György Vámosi [c,**], Miroslav Almáši [d,**]

[a] Center for Interdisciplinary Biosciences, Technology and Innovation Park, P.J. Šafárik University in Košice, Jesenná 5, SK-041 54 Košice, Slovak Republic
[b] Institute of Animal Biochemistry and Genetics, Centre of Biosciences, Slovak Academy of Sciences, Dúbravská cesta 9, SK-840 05 Bratislava, Slovak Republic
[c] Department of Biophysics and Cell Biology, Faculty of Medicine, University of Debrecen, Doctoral School of Molecular Medicine, Egyetem tér 1, H-4032 Debrecen, Hungary
[d] Department of Inorganic Chemistry, Faculty of Science, P. J. Šafárik University in Košice, Moyzesova 11, SK-041 54 Košice, Slovak Republic
[e] BovaChem s.r.o, Laboratory-1, Kirejevská 22, SK-979 01 Rimavská Sobota, Slovak Republic
[f] Department of Biophysics, Faculty of Science, P. J. Šafárik University in Košice, Jesenná 5, SK-041 54 Košice, Slovak Republic
[g] Laboratory for Functional and Metabolic Imaging, Institute of Physics, Swiss Federal Institute of Technology in Lausanne (EPFL), Station 3, Building PH, CH-1015 Lausanne, Switzerland
[h] Department of Chemistry, Faculty of Science, University of Ostrava, 30. Dubna 22, CZ-702 00 Ostrava, Czech Republic
[i] Institute of Experimental Physics, Slovak Academy of Sciences, Watsonova 47, SK-040 01 Košice, Slovak Republic
[j] Depart of Condensed Matter Physics, Faculty of Science, P. J. Šafárik University in Košice, Jesenná 5, SK-041 54 Košice, Slovak Republic
[k] Department of Biochemistry, Faculty of Science, P. J. Šafárik University in Košice, Moyzesova 11, SK-041 54 Košice, Slovak Republic

## HIGHLIGHTS

- Metal-organic framework MIL-101(Al)–$NH_2$ was developed for bioimaging and drug delivery.
- The interaction of hypericin and MIL-101(Al)–$NH_2$ with the spike protein SARS-CoV-2 RBD-SD1 was investigated.
- The interaction of hypericin and MIL-101(Al)–$NH_2$ with angiotensin-converting enzyme 2 receptors in cells was investigated.
- The photodynamic activity of the prepared construct was demonstrated in cells and bacteria.

## GRAPHICAL ABSTRACT

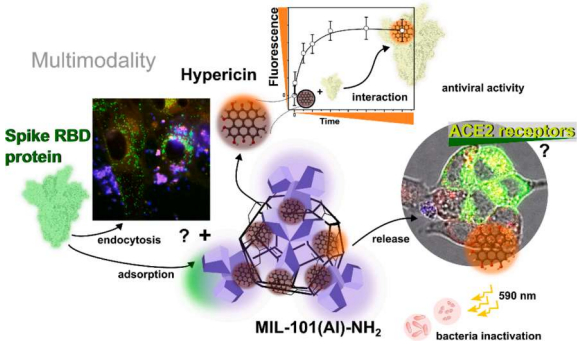


* Corresponding author at: Center for Interdisciplinary Biosciences, Technology and Innovation Park, P.J. Šafárik University in Košice, Jesenná 5, SK-041 54 Košice, Slovak Republic.
** Corresponding authors.
*E-mail addresses:* veronika.huntosova@upjs.sk (V. Huntošová), vamosig@med.unideb.hu (G. Vámosi), miroslav.almasi@upjs.sk (M. Almáši).

https://doi.org/10.1016/j.jcis.2025.137454
Received 27 January 2025; Received in revised form 23 March 2025; Accepted 26 March 2025
Available online 26 March 2025

ARTICLE INFO

*Keywords:*
MIL-101(Al)–$NH_2$
Hypericin
ACE2 receptors
RBD spike protein
Photodynamic therapy
Selectivity

ABSTRACT

The global pandemic of SARS-CoV-2 has highlighted the necessity for innovative therapeutic solutions. This research presents a new formulation utilising the metal–organic framework MIL-101(Al)–$NH_2$, which is loaded with hypericin, aimed at addressing viral and bacterial challenges. Hypericin, recognised for its antiviral and antibacterial efficacy, was encapsulated to mitigate its hydrophobicity, improve bioavailability, and utilise its photodynamic characteristics. The MIL-101(Al)–$NH_2$ Hyp complex was synthesised, characterised, and evaluated for its biological applications for the first time. The main objective of this study was to demonstrate the multimodal potential of such a construct, in particular the effect on SARS-CoV-2 protein levels and its interaction with cells. Both *in vitro* and *in vivo* experiments demonstrated the effective transport of hypericin to cells that express ACE2 receptors, thereby mimicking mechanisms of viral entry. In addition, hypericin found in the mitochondria showed selective phototoxicity when activated by light, leading to a decrease in the metabolic activity of glioblastoma cells. Importantly, the complex also showed antibacterial efficacy by selectively targeting Gram-positive *Staphylococcus epidermidis* compared to Gram-negative *Escherichia coli* under photodynamic therapy (PDT) conditions. To our knowledge, this study was the first to demonstrate the interaction between hypericin, MIL-101(Al)–$NH_2$ and the receptor-binding domain (RBD) of the SARS-CoV-2 spike protein, which inhibits cellular uptake and colocalises with ACE2-expressing cells. Therefore, the dual functionality of the complex – targeting the viral RBD and the antibacterial effect via PDT – emphasises its potential to mitigate complications of viral infections, such as secondary bacterial infections. In summary, these results suggest that MIL-101(Al)–$NH_2$ Hyp is a promising multifunctional therapeutic agent for antiviral and antibacterial applications, potentially contributing to the improvement of COVID-19 treatment protocols and the treatment of co-infections.

## 1. Introduction

The COVID-19 pandemic, which emerged in December 2019, has presented significant challenges and raised new questions regarding the effective combat of coronavirus diseases. Severe acute respiratory syndrome coronavirus 2 (SARS-CoV-2) is still circulating in the population and causes different complications that can lead to long-lasting side effects [1]. Despite the great efforts made by the medical and scientific community, there are still many unsolved problems that should be thoroughly investigated.

The rapid determination of the structure of SARS-CoV-2 [2] facilitated the identification of the mechanism by which the virus recognises the target cells of the organism [3]. SARS-CoV-2 bind to angiotensin-converting enzyme 2 receptors (ACE2r), which facilitate entry of the virus into the cells. Attachment of the virion to the host cell membrane is mediated by spike glycoproteins assembled into a homotrimer. It is present in multiple copies on the virion membrane that makes a crown-like form. The original spike protein fragments of the Wuhan-Hu-1 strain create complexes of ACE2r through the receptor binding domain (RBD) [2].

The transport mechanism of the virion can be characterised by active transport such as micropinocytosis, caveolar/lipid raft and clathrin-mediated endocytosis [4]. Many membranous structures of different sizes originated from the endoplasmic reticulum were recognised in infected cells with electron microscopy [5,6]. It was reported that synthesised viral proteins and genomic RNA translocate to the endoplasmic reticulum and the Golgi apparatus intermediate compartment (ERGIC) for virus assembly and budding [6,7]. Here, the spike protein is heavily glycosylated, which affects its folding, stability, and sensitivity in interacting with ACE2r [8].

After attachment of the virus to the plasma membrane of the host cells, it is cleaved by the transmembrane serine protease 2, resulting in activation of the spike protein and initiation of the fusion process of the viral membrane with the host cell plasma membrane. In the absence of transmembrane serine protease 2 it is cleaved by cathepsin B and L inside the lysosome lumen [9]. Mykytyn and coworkers revealed that the inhibition of serin protease can be a potential strategy to prevent SARS-CoV-2 entry and replication in host cells [10].

The replication cycle of SARS-CoV-2 is controlled at different stages with various proteases that can serve as the targets for the treatment. The main protease, 3-chymotrypsin-like protease, is responsible for processing viral polyproteins into non-structured proteins [11], and it is critical for the replication of coronaviruses [12].

Hypericin, an anthraquinone that can be naturally obtained from plants of the genus *Hypericum*, possesses interesting antiviral activity against some viruses [13,14]. Moreover, it was demonstrated that hypericin has antibacterial [15,16] and anticancer [17–19] efficacy. In recent years, this molecule has gained attention for its potential to inhibit SARS-CoV-2.

With *in silico* methods, Thang and coworkers demonstrated that hypericin binds to 3-chymotrypsin-like protease through two pockets [20]. They complemented the results of molecular docking with a fluorescence resonance energy transfer study that confirmed inhibition of the 3-chymotrypsin-like protease activity with hypericin and *in vitro* proved that hypericin inhibits viral intracellular replication.

Matos et al. reported that hypericin binds with high affinity to viral main-protease and RNA-dependent RNA polymerase. They demonstrated Hypericin activity in a dose-dependent manner for anti-SARS-CoV-2 replication in an *in vitro* model of Vero-E6 infected cells. Hypericin was identified as an excellent candidate for repurposing for the treatment of COVID-19, with possible inhibition of two important phases of virus maturation [21].

Delcanale et al. demonstrated that hypericin binds to the membrane envelope of SARS-CoV-2 with a strong affinity, where 30 molecules of hypericin can be loaded on a single viral particle [22]. They also showed a significant reduction of the viral infectivity toward Vero E06 cells in the dark and after irradiation.

Bajrai et al. screened the antiviral properties of *Hypericum perforatum* using Vero E6 cells [23]. They measured the inhibition of viral load using quantitative real-time polymerase chain reaction on cell culture assay. They showed that *H. perforatum* possesses significant antiviral and virucidal effects.

Despite the promising potential of hypericin in the treatment protocols, the main obstacles are affiliated with the highly hydrophobic character that makes it insoluble in aqueous solutions [24,25] and decreases its biological activity [26,27]. However, this, in particular, can be overcome by encapsulation of this molecule to increase its bioavailability and biological activity, which can be amplified by the application of light in photodynamic treatment (PDT) [28–31]. PDT employed light-activated hypericin that interacts with molecular oxygen in its excited triplet state to create reactive oxygen species, resulting in the elimination of the targeted cells and tissues [32].

One of the side effects of SARS-CoV-2 infection that was reported in many clinical studies is secondary serious bacterial infection, often

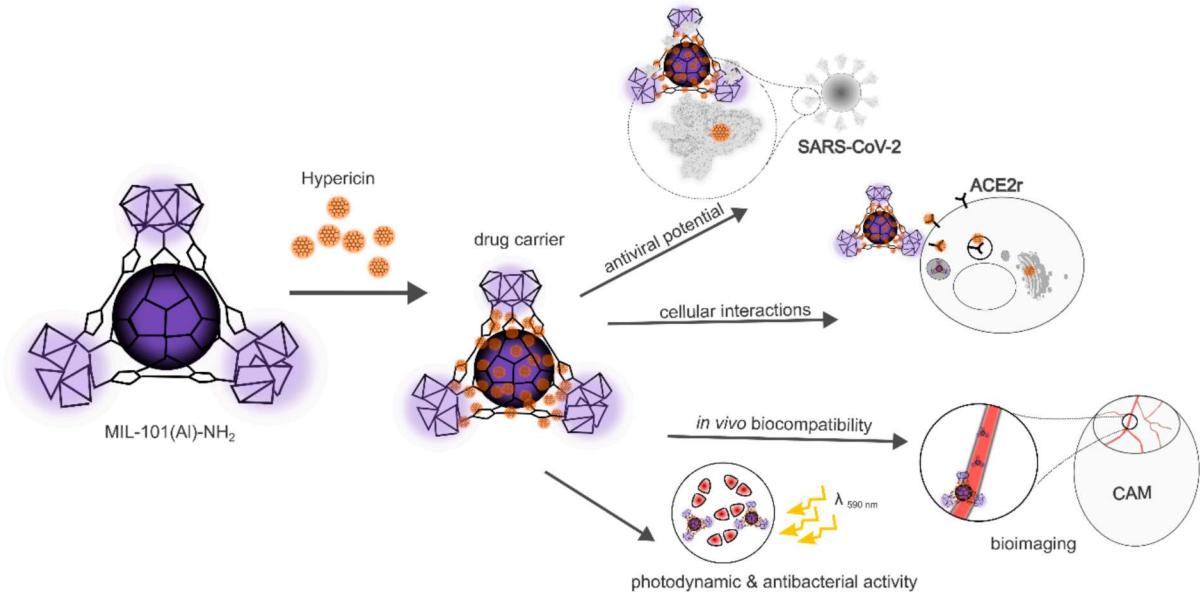


**Fig. 1.** Schematic representation of the experimental setup and the multimodal activity of MIL-101(Al)–$NH_2$ loaded with hypericin.

resulting in fatal consequences [33–35]. PDT can be an elegant modality to inhibit viral replication and antibacterial treatment with the same drug composition [36].

Porous materials are very attractive as nanocarriers for hydrophobic and hydrophilic molecules, including hypericin [31,37]. Metal-organic frameworks (MOFs) represent a promising class of highly porous nanocarriers for biomedical applications with excellent thermal, chemical and mechanical stability [38,39]. The composition of MOFs can be tuned by combining organic ligands and metal ions through coordination bonds or postsynthetic modification [40].

MIL-101, as a mesoporous material, has proven to be ideal for drug delivery applications due to its exceptional surface area and large pore size that facilitates efficient drug loading and release [41,42]. Since its discovery in 2005 [43], many analogues of MIL-101 have been prepared by using metal nodes with a (+III) oxidation state, such as Cr, Fe, and Al, along with various derivatives of terephthalic acid [44]. These modifications have allowed for the tuning of the framework's properties, such as stability, pore size, and functionality, expanding the material's potential for various applications, including drug delivery. By adjusting the central metal ions and organic linkers, researchers have been able to optimize the structure for specific uses [45,46]. MIL-101(Al)–$NH_2$, composed of aluminium(III) ions and a 2-aminoterephthalate linker, offers significant advantages for biomedical applications compared to its counterparts based on chromium(III) and iron(III) analogues. One of its primary benefits is its biocompatibility and low toxicity, which are crucial for applications in drug delivery. Unlike MIL-101(Cr)–$NH_2$, which, despite its high stability, poses potential health risks due to its oxidation and the toxicity of Cr(VI) species [47], MIL-101(Al)–$NH_2$ is considered safer for direct biomedical use. In comparison to MIL-101(Fe)–$NH_2$, the aluminium(III)-based variant offers greater stability in biological environments, as iron(III)-based MOF-101 may undergo redox reactions, potentially leading to structural degradation and oxidative stress in living systems [48]. The low atomic weight of aluminium(III) as the central ion, and consequently the low molecular weight of the resulting porous material, must also be considered. This characteristic provides an advantage in terms of specific properties, such as surface area or drug storage capacity, which are related to per gram of the material. Moreover, the amine (–$NH_2$) functional groups present in MIL-101(Al)–$NH_2$ further enhance its biomedical potential by promoting strong interactions with biomolecules, improving drug loading efficiency, and enabling targeted delivery. Amine groups can act as Lewis bases and significantly influence oxidation–reduction reactions [49]. Xu and Yan reported that amine functionalisation of MIL-101(Al)–$NH_2$ improves the luminescence of this material, which is also *pH*-dependent and can serve as a sensor under certain conditions [50]. These attributes position MIL-101(Al)–$NH_2$ as a promising candidate for drug delivery applications, highlighting its potential in the development of advanced drug carrier systems.

MOF materials contribute to the fight against SARS-CoV-2 and COVID-19 at multiple levels, ranging from sample preparation and detection to viral elimination [39]. It has been demonstrated that MOF materials, such as ZIF-90 [51], can enhance the stability of COVID-19 serological tests. In the field of virus detection, various MOFs have been explored, including ZIF-8 [52,53], Y(III) [54], and Eu(III) or Tb(III)-MOFs based on a 5-(4-(imidazol-1-yl) phenyl) isophthalate linker [55], which facilitate rapid and sensitive COVID-19 diagnosis through fluorescence or luminescence changes. Moreover, the surfaces of three MOFs, UiO-66, UiO-66-$NH_2$, and UiO-66-$NO_2$, have been functionalized with repurposed antiviral agents, specifically folic acid, nystatin, and tenofovir, to enable targeted interactions with the external spike protein of the SARS virus. Protein-binding studies have demonstrated that this surface modification significantly enhances the affinity for both glycosylated and non-glycosylated proteins, leading to the deactivation of respiratory coronaviruses [56]. Additionally, Dahri et al. investigated the interaction of MOF materials from ZIF and IR-MOF families with the main protease and their potential role in inhibiting spike protein binding to ACE2r through in silico analysis [57]. Furthermore, the elimination of SARS-CoV-2 has been studied using UiO-66, HKUST-1, MIL-53, and MIL-125 [58], where viral degradation was achieved through oxidative-reductive mechanisms and light-driven photocatalytic processes.

In the present study, hypericin was loaded into MIL-101(Al)–$NH_2$ with the aim of transporting this hydrophobic molecule into the vicinity of cells expressing ACE2r. The aim of this transport was to enable the interaction of hypericin with the target cells (and thus mimic the entry and infection with the SARS-CoV-2 virus). For this reason, the interaction of the MOF complex with ACE2r-positive cells and the spike protein of the virus was analysed at the molecular and cellular level using fluorescence spectroscopy and microscopy. Finally, the multiple applications of these materials, including photodiagnostics and photodynamic therapy, were demonstrated *in vivo* (preclinical model of chicken embryo chorioallantoic membrane (CAM)) and *in vitro* at the cellular and bacterial levels (schematic representation is shown in Fig. 1).

## 2. Material and methods

### 2.1. Synthesis of the MIL-101(Al)–$NH_2$ particles and their conjugation with hypericin

In the typical synthesis of MIL-101(Al)–$NH_2$ reported in [59,60], 300 mg (1.656 mmol) of 2-aminoterephthalic acid and 250 mg (0.666 mmol) of $Al(NO_3)_3{\cdot}9H_2O$ were dissolved in 15 mL of *N,N*-dimethylformamide (DMF) using ultrasound-assisted dispersion. The resulting clear solution was transferred to a glass vial and heated in an oven at 110 °C for 24 h. The light beige solid product obtained was filtered and washed with three portions (20 mL each) of methanol. To remove excess 2-aminoterephthalic acid and $Al(NO_3)_3{\cdot}9H_2O$, the crude material was purified using a Soxhlet extractor for 24 h with methanol as the solvent. After extraction, 350 mg of the pure final product MIL-101(Al)–$NH_2$ was obtained.

The drug-loaded material, MIL-101(Al)–$NH_2$ Hyp, was prepared by an impregnation method using a methanolic solution of hypericin (Hyp, abcam, Cambridge, United Kingdom). MIL-101(Al)–$NH_2$ was activated at 100 °C for 30 min prior to impregnation to remove solvent molecules from the cavities. Then, 10 mL of methanolic hypericin solution at a mass concentration of 10 mg $L^{-1}$ was added to 500 mg of activated material. The methanol was freely evaporated at ambient temperature, while the drug was encapsulated in the channel system of the porous material due to capillary forces. To ensure efficient storage of hypericin, 5 mL of pure methanol was subsequently added to dissolve the trace amounts of the drug on the grain surface and transport it into the pore. This process was repeated a total of 3 times. By the impregnation procedure described above, 0.2 mg of Hyp was stored in 1 g of MIL-101(Al)–$NH_2$.

### 2.2. Stability and characterization of unmodified and drug-loaded MIL-101(Al)–$NH_2$

Prepared samples were characterised by Fourier transform infrared spectroscopy (FTIR) measured on a Nicolet 6700 instrument from Thermo Scientific, USA. Measurements of the materials were performed by transmittance technique using KBr tablets with a sample weight ratio of 100: 1 in the wavelength range from 4000 to 400 $cm^{-1}$ with 32 scans at a resolution of 4 $cm^{-1}$. Simultaneous thermogravimetric analysis and differential scanning calorimetry (TG/DSC) measurements were performed using the SetsysEvolution instrument from Setaram, France. The experiments with approx. 10 mg of samples were conducted in $\alpha$-$Al_2O_3$ crucibles under an air atmosphere consisting of 20 % $O_2$ and 80 % Ar with a total flow rate of 40 mL $min^{-1}$. The TG/DSC experiments were conducted according to the following temperature programme: heating from 30 °C to 80 °C (10 °C $min^{-1}$), an isothermal step at 80 °C for 30 min (to remove excess solvent), heating to 900 °C (10 °C $min^{-1}$). Nitrogen adsorption and desorption at −196 °C were measured using an ASAP 2020 instrument from Micromeritics, USA. Prior to adsorption studies, the samples were activated at 100 °C for 24 h under vacuum to remove solvents from the pores. Nitrogen adsorption isotherms for the activated samples were measured in the relative pressure range of $p/p_0 = 0.005$ to 1, based on which the specific surface areas ($S_{BET}$) were evaluated according to the BET equation. Pore volumes ($V_p$) and sizes ($d$) of the samples were evaluated using the BJH method, from the desorption branches of isotherms [61]. Powder X-ray diffraction (PXRD) measurements were applied to analyse the crystal structure, stability and determine the grain sizes of the prepared materials. The analysis was carried out on a D2 PHASER diffractometer from Bruker, USA, using CuKα radiation ($\lambda$ = 1.54056 Å) in the $2\theta$ range from 10 to 50°. The stability, morphology, and particle size of MIL-101(Al)–$NH_2$ were investigated and determined using scanning electron microscopy (SEM) with a TESCAN MIRA3 instrument (TESCAN, Brno, Czech Republic) equipped with an auto-emission cathode. The chemical composition and elemental distribution mapping of the materials were analyzed using energy-dispersive X-ray (EDX) spectroscopy on an EDAX X-act system (Oxford Instruments, UK). The material grains were deposited onto an adhesive carbon tape affixed to a sample holder, which was subsequently inserted into the instrument for measurement. The particle size of MIL-101(Al)–$NH_2$ was calculated from the SEM image using Image J software [62]. The total released amount of hypericin in phosphate-buffered saline (PBS) at $pH$ = 7.4 and fetal bovine serum (FBS, biosera, Nuaille, France) media was measured in 1 nm steps. The fluorescence spectra of released hypericin were collected in the range of 500–700 nm at 488 nm excitation using a fluorescence spectrophotometer (Jasco FP-8550, Kyoto, Japan).

### 2.3. Release of hypericin from MIL-101(Al)–$NH_2$ particles

The release of hypericin was carried out as follows: 50 mg of MIL-101(Al)–$NH_2$ Hyp containing 10 μg of hypericin (0.2 mg $g^{-1}$) was weighed into 50 mL plastic vials. The release process was conducted in PBS with a $pH$ of 7.4. Samples were collected and measured at time intervals of 0.25, 0.5, and 1 h. Subsequently, 20 mL of a 10 % FBS solution was added, as the formation of hypericin monomers through FBS ensures the solubility of hypericin in aqueous environments. Additional sampling was performed at 2, 3, 4, 5, 6, and 24 h. The detection of hypericin was carried out using a fluorescence spectrophotometer at $\lambda_{max}$ = 599 nm, with quantification based on a calibration curve defined by the equation $y = 0.03x - 0.0793$ ($R^2 = 0.9999$), in which $y$ is fluorescence intensity, and $x$ is known concentration of hypericin.

### 2.4. MIL-101(Al)–$NH_2$ stability study

The stability of MIL-101(Al)–$NH_2$ upon immersion in various solutions was systematically investigated in this study. Dimethyl sulfoxide (DMSO), phosphate-buffered saline (PBS), and fetal bovine serum (FBS) were selected as testing media. To simulate conditions used in biological assays, 100 mg of the pure material was mixed with each solution and continuously stirred for 48 h at 37 °C. Following the incubation period, the material was filtered, air-dried at ambient temperature, and subsequently analyzed using powder X-ray diffraction (PXRD), infrared spectroscopy (IR), and scanning electron microscopy (SEM) coupled with energy-dispersive X-ray spectroscopy (EDX).

### 2.5. Fluorescence spectroscopic characterisation of MIL-101(Al)–$NH_2$ particles

The excitation-emission matrices of the 0.01 mg/mL MIL-101(Al)–$NH_2$ and MIL-101(Al)–$NH_2$ Hyp samples in distilled water were measured with a spectrofluorometer (Horiba Jobin-Yvon FluoroLog-3, Germany). Excitation was performed in the spectral range of 250–600 nm and emission at 300–800 nm. This device can also be operated in a time-resolved mode for measure the fluorescence lifetime. The excitation source for the fluorescence lifetime measurements was a NanoLED (405 nm), and the detection was performed by time-correlated single photon counting. The acquired fluorescence decay data were analysed with the DAS6 software (Horiba Jobin-Yvon, Germany) using a bi-exponential function fitting module.

### 2.6. Biodistribution and in vivo biocompatibility of MIL-101(Al)–$NH_2$ and hypericin in the CAM model

Fertilised chicken eggs (Animalco AG, Switzerland) were placed in an automatic rotary incubator (FIEM snc, Italy). The eggs were kept in the incubator for 3 days at 37 °C, atmospheric oxygen pressure (155.4 mm Hg) and relative humidity of 65 % with the blunt end upwards. On the embryonic development day (EDD) 3, a small portion of the shell was removed at the sharp end to create a hole (~ 3 mm diameter). This area was then covered with adhesive tape (Scotch® Magic™, St. Paul, Minnesota, USA). The eggs were then incubated in a static position until

the experiments. On EDD 11, the perforated area in the shell was enlarged (~2.5 cm diameter).

A volume of 50 μL containing 1 mg/mL MIL-101(Al)–$NH_2$ and MIL-101(Al)–$NH_2$ Hyp saline (0.9 % NaCl) was injected into the main vein of the CAM. The perforation was covered with a Parafilm M barrier film (Pechiney Plastic Packaging Company, Chicago, Illinois, USA). The biocompatibility of the substances was evaluated 24 h after intravenous administration of 20 μL of 20 kDa dextran-FITC (25 mg/mL saline). Capillary occlusion was considered as mild damage to the CAM.

Imaging of the CAM was performed immediately after injection of the compounds using an *epi*-fluorescence microscope (Nikon Eclipse E600 FN, Nikon, Japan) equipped with a Hg arc lamp (HBO 103 W/2, Osram, Germany), a 4×/0.13 objective (Plan Fluor ∞/−, Nikon, Japan), and a filter cube with excitation 365/10, emission filtered by DM400 and BA410. The fluorescence images were recorded 120 s after administration. The injection of the solution was recorded with a Huawei BLA-L29 camera system (Huawei, Shenzhen, China). The fluorescence intensity was determined from the colour images and evaluated using the ImageJ software.

### 2.7. Cell cultures and preparation of ACE2 EGFP HEK cell model

Human glioblastoma cells U87MG (purchased from Cells Lines Services, Eppelheim, Germany) were cultured in Dulbecco's modified Eagle medium (D-MEM, high glucose, GlutaMAX™, with pyruvate, Gibco-Invitrogen, Life Technologies Ltd., Paisley, UK). Human dermal fibroblasts HDF (purchased from Cell, Applications, San Diego, CA) were grown in RPMI 1640 (Biosera, Nuaille, France). The cell culture medium was supplemented with 10 % fetal bovine serum (FBS, Biosera, Nuaille, France) and streptomycin-penicillin (1 % w/w, Gibco-Invitrogen) according to the propagation protocol.

Human embryonic kidney cell line HEK293T (ATCC, Manassas, Virginia, USA) was maintained in complete 10 % FBS D-MEM and 50 mg/L gentamicin (KARA, Novo Mesto, Slovenia). For the microscopy experiments, HEK293T cells were subcultured in 8-well chambered coverslips (ibidi, Munich, Germany) and maintained in a phenol red-free medium. Twenty-four hours after seeding, the cells reached 50–60 % confluency and were transiently transfected with 75–80 ng of ACE2-EGFP using the FuGENE® HD transfection reagent (Promega, MA, USA), as recommended by the manufacturer. The cells were used for microscopy within 24 h after the transient transfection.

The particles were dispersed in distilled water at a concentration of 1 mg/mL, and the aliquots were added to the cell culture medium for different periods of time according to the experimental procedures. Prior to administration, the particles were sonicated for 5 min.

### 2.8. Flow cytometry analysis of MIL-101(Al)–$NH_2$ uptake by U87MG cells and their interaction with spike protein

U87MG cells were cultured with 0.2 mg/mL MIL-101(Al)–$NH_2$ and hypericin-loaded particles for 24 h. The uptake of particles and hypericin by U87MG cells was detected using the CytoFlex S analyser (Beckman Coulter, Brea, California, United States) in channels V450 (particles) and Y610 (hypericin).

To mimic the penetration of SARS-CoV-2 into the cells, the spike protein SARS-CoV-2 RBD-SD1 (Friedrich-Loeffler-Institut, Greifswald-Insel Riems, Germany) conjugated with AlexaFluor 488 (ThermoFisher Scientific, Waltham, MA, USA) was added to the cell culture medium for 1 h. The SARS-CoV-2 RBD-SD1 protein was labelled with AlexaFluor 488 for 50 min and separated with Sephadex G50 (ThermoFisher Scientific). The mixture of the spike protein with 0.2 mg/mL MIL-101(Al)–$NH_2$ Hyp was stabilised for 1 h and added to the cell for 1 h. The cells were detached after incubation and measured in a cold phosphate saline solution. The histograms and correlation diagrams of channels B525 (spike protein fluorescence) and Y610 (hypericin fluorescence) were recorded.

### 2.9. Interaction of particles with SARS-CoV-2 RBD-SD1

The SARS-CoV-2 RBD-SD1 conjugated with AlexaFluor 488 were prepared in phosphate-buffered saline (PBS, $pH = 7.4$) at concentrations 0.0017 and 0.0013 mg/mL, respectively. Hypericin at a concentration of 600 nM was added to these solutions, and the fluorescence of tryptophan and AlexaFluor 488 was detected using the fluorescence spectrometer Jasco FP-8550 (Tokyo, Japan) for 300 min. Alternatively, 600 and 33 nM hypericin solutions in PBS were prepared, and SARS-CoV-2 RBD-SD1 was added to allow binding. The fluorescence maximum was detected at 300 nm (excitation at 280 nm) for tryptophan, 520 nm (excitation at 488 nm) for AlexaFluor 488, and 600 nm (excitation at 555 nm) for hypericin.

### 2.10. Confocal fluorescence intensity and lifetime imaging of MIL-101 (Al)–$NH_2$ and hypericin in cells

Fluorescence and bright field images of HEK293T cells, transfected with ACE2-EGFP and particles were acquired using a confocal fluorescence microscope A1 (Nikon, Tokyo, Japan) equipped with a Plan-Apochromat 60×/NA 1.27 water immersion objective and a time-correlated single photon counting upgrade kit (PicoQuant, Berlin, Germany) to detect fluorescence lifetime images. Particles were excited with a 405 nm pulsed laser, EGFP with a 485 nm laser, and hypericin with a 561 nm laser. Emissions were detected using a PMA Hybrid 40 detectors in the appropriate spectral range: 482/35 nm, 525/35 nm, 600/50 nm. Fluorescence decay curves were fitted with the SymphoTime 64 software to a multiexponential reconvolution model with 2-lifetime components.

U87MG cells exposed to particles and spike protein were detected with an LSM 900 microscope using an Airyscan 2 detector (ZEISS) for multiplexing super-resolution and higher sensitivity in sample scanning. To collect the images in super-resolution mode, a Plan-Apochromat 63x/1.4 Oil DIC M27 objective (ZEISS) was used. Post-processing analysis was done with the Joint deconvolution (ZEISS) plugin. Excitation was acquired as follows: 405 nm for particle detection (400–505 nm emission detection), 488 nm for AlexaFluor 488 (450–545 nm emission detection) and 561 nm for hypericin and MitoSOX™ red (Thermofisher Scientific) mitochondrial superoxide indicator (570–700 nm) detection. ZEISS ZEN 3.10 software was used for image analysis.

The colocalisation analysis was carried out using the ImageJ software with the colocalisation plugin. The number and size of vesicles/areas in the images processed with a threshold were calculated using the same software using the measure particles plugin.

### 2.11. Phototoxicity induced by MIL-101(Al)–$NH_2$ and hypericin in cells

U87MG cells were cultured for 3 h with 0.1, 0.2 and 0.5 mg/mL MIL-101(Al)–$NH_2$ and MIL-101(Al)–$NH_2$ Hyp particles. Then, these cells were irradiated with 590 nm light at 2 and 10 J/cm$^2$ (2 and 10 min). The cells were then kept in an incubator at 37 °C in the dark for 24 h. Alternatively, these cells with the particles were kept in the dark for 24 h. The control group was not exposed to the particles but was irradiated or kept in the dark. After this incubation, the 3-(4,5-dimethylthiazol-2-yl)-2,5-diphenyltetrazolium bromide (MTT, Sigma-Aldrich, Germany) was added to the cell culture medium for 1 h. The medium was then removed, and the formazan crystals were dissolved in DMSO and measured at 560 nm using a plate reader. The background at 700 nm was subtracted, and the percentage of formazan production compared to controls was determined. Formazan production is related to mitochondrial metabolic activity and reflects cell viability.

### 2.12. Determination of statistical significance

Statistical analysis of the results was performed using an one-way ANOVA test: *$p < 0.05$, **$p < 0.01$ and ***$p < 0.001$.

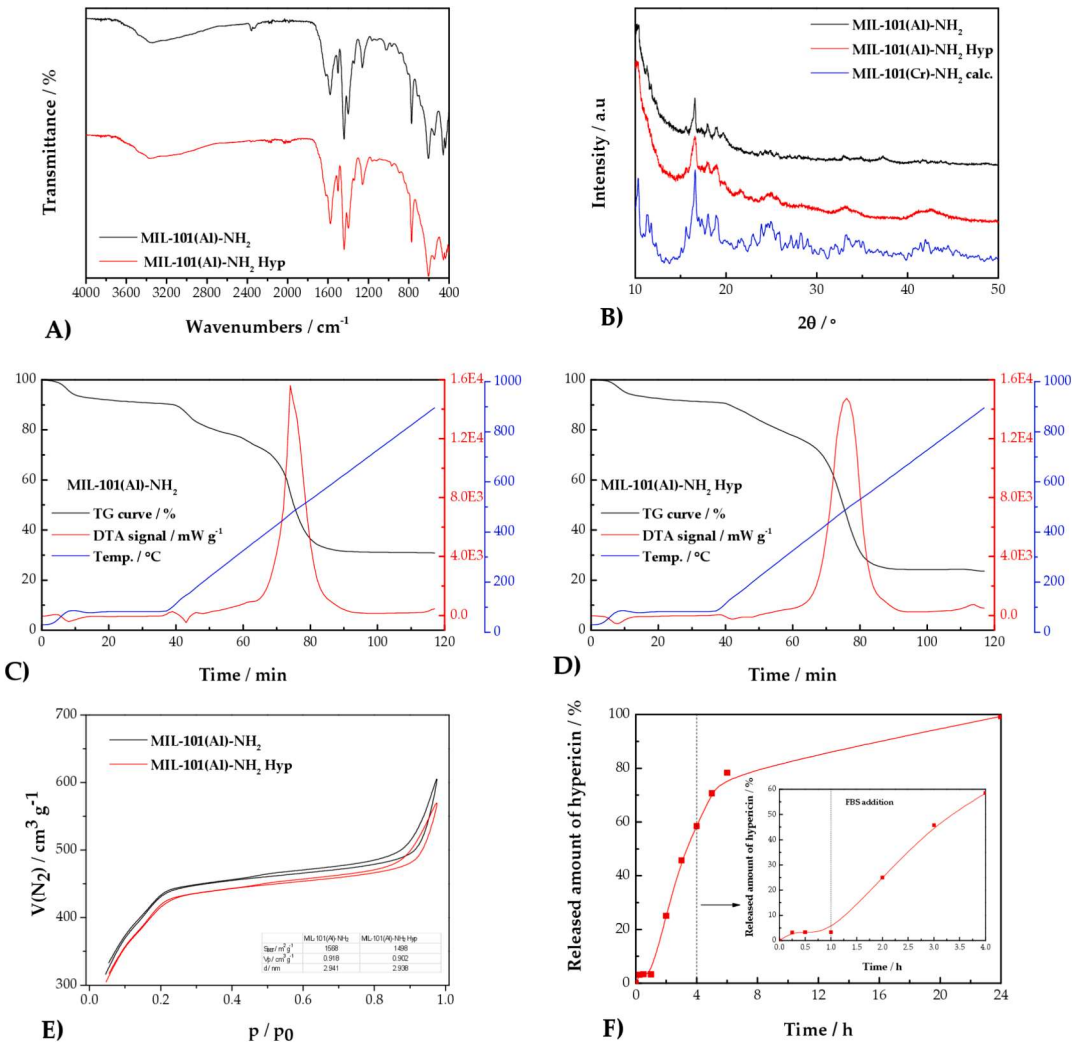


**Fig. 2.** Physico-chemical analysis results of prepared samples (MIL-101(Al)–$NH_2$ and MIL-101(Al)–$NH_2$ Hyp): (A) Fourier transform infrared spectra; (B) measured and calculated PXRD patterns. Thermogravimetric analysis coupled with differential thermal analysis for (C) pristine material and (D) hypericin-loaded sample. (E) Nitrogen adsorption/desorption isotherms measured at −196 °C (inset shows the calculated textural parameters: ($S_{BET}$ in $m^2\ g^{-1}$), pore volume ($V_p$ in $cm^3\ g^{-1}$) and diameter ($d$ in nm). (F) The release kinetics of hypericin from the porous MIL-101(Al)–$NH_2$ matrix in PBS (up to 1 h) and FBS (at 1–24 h intervals). The inset shows a closer view of the hypericin release profile in the interval 0–4 h.

### *2.13. Bacterial culture and photodynamic antibacterial treatment mediated with MIL-101(Al)–$NH_2$ and hypericin*

Bacterial strains, *Escherichia coli* CCM 3954 (*E. coli* in further) and *Staphylococcus epidermidis* CCM 4418 (*S. epidermidis* in further) were obtained from the Czech Collection of Microorganisms (Masaryk University, Brno, Czech Republic). To generate a culture, the strains were grown in Mueller Hinton broth (ThermoFisher Scientific) at 37 °C and 250 rpm overnight. The cultures were then diluted in Mueller Hinton broth to an optical density at 600 nm of 0.2, and three independent 2 mL samples were prepared for each strain: negative control (without nanoparticles), MIL-101(Al)–$NH_2$ Hyp kept in the dark and irradiated. The particles were added to bacterial culture in a final concentration of 1 mg/mL and incubated at 37 °C and 250 rpm for 2 h. Following incubation, the samples were irradiated with a LED light source at 500 nm and a light dose of 10 J/$cm^2$ for 10 min. Finally, ten-fold serial dilutions in Mueller Hinton broth were prepared from each sample (up to $10^{-7}$), and 10 µL spots were plated on Mueller Hinton agar plates and allowed to dry in a biosafety cabinet. Plates were incubated overnight at 37 °C. All experimental work was performed under low-light conditions.

## 3. Results and discussion

### *3.1. MIL-101(Al)–$NH_2$ and MIL-101(Al)–$NH_2$ Hyp particles characterization*

The prepared MIL-101(Al)–$NH_2$ and hypericin-loaded MIL-101(Al)–$NH_2$ Hyp materials, and pure Hypericin were initially characterised using infrared spectroscopy. As shown in Fig. 2A, the IR spectra of the pure MOF (black spectrum) and the hypericin-loaded MOF (red spectrum) exhibit several absorption bands corresponding to the molecular structures of MIL-101(Al)–$NH_2$ and MIL-101(Al)–$NH_2$ Hyp. The absorption bands associated with the linker, 2-aminoterephthalate, are observed at 3487 $cm^{-1}$ and 3363 $cm^{-1}$, corresponding to asymmetric $\nu(N—H)_{as}$ and symmetric $\nu(N—H)_s$ stretching vibrations, respectively. Moreover, the deformation scissoring $\delta(N—H)$ vibration appears at 1622 $cm^{-1}$. Additionally, the stretching vibration for $\nu(C—N)$ is located at 1258 $cm^{-1}$. Characteristic vibrations of the aromatic ring are observed at 1437 $cm^{-1}$ and 1506 $cm^{-1}$, corresponding to $\nu(C—C)_{ar}$ stretching. The carboxylate anions exhibit asymmetric $\nu(COO^-)_{as}$ and symmetric $\nu(COO^-)_s$ stretching vibrations at 1578 $cm^{-1}$ and 1401 $cm^{-1}$, respectively [63]. Finally, the absorption band at 605 $cm^{-1}$ confirms the presence of a coordinated linker to Al(III) central ions through the $\nu$(Al-

O) stretching vibration. Evidence for hypericin (IR spectrum of pure hypericin is shown in Fig. S1 in ESI) loaded into MIL-101(Al)–$NH_2$ can be found at 2000 $cm^{-1}$, which corresponds to aromatic overtones. Due to the higher presence of aromatic rings in the measured sample, these overtones can be observed [64]. By comparing the IR spectra of pure hypericin and the Hyp-loaded sample, no additional absorption bands corresponding to hypericin can be identified in the spectrum of the MIL-101(Al)–$NH_2$ Hyp material. The amount of hypericin stored within the carrier's pores (0.2 mg of hypericin per 1 g of MIL-101(Al)–$NH_2$) is too low to produce distinct and characteristic absorption bands. At this concentration, the sensitivity of the instrumental technique used is insufficient for the detection and detailed characterization of hypericin.

The powder X-ray diffraction (PXRD) analysis was performed to confirm the crystal structure of MIL-101(Al)–$NH_2$ and evaluate the stability of the drug carrier after hypericin encapsulation (see Fig. 2B). The PXRD patterns of both samples were compared with the powder diffraction record calculated from the single-crystal X-ray diffraction data of MIL-101(Cr)–$NH_2$ [43]. A closer examination of the PXRD patterns shows excellent agreement with the calculated diffractogram, indicating that the compound was prepared correctly and contains the desired cubic MIL-101 framework. Moreover, because of the similarity between the MIL-101(Al)–$NH_2$ and MIL-101(Al)–$NH_2$ Hyp PXRD patterns, it can be concluded that the crystal lattice remains stable after hypericin encapsulation. This stability is evidenced by the unaltered diffraction pattern when compared to MIL-101(Al)–$NH_2$. Interestingly, the broadening of peaks observed after adsorption suggests a reduction in crystallinity due to the formation of an amorphous hypericin layer in the pores of MIL-101(Al)–$NH_2$ [65] According to previous study [66], the crystallite size calculated using the Debye-Scherrer equation was 39.7 nm for MIL-101(Al)–$NH_2$ and 28.9 nm for MIL-101(Al)–$NH_2$ Hyp. This phenomenon is attributed to the adsorption of hypericin into the mesoporous structure of MIL-101(Al)–$NH_2$, leading to structural disorders and crystal defects – typical characteristics of the drug adsorption onto metal–organic frameworks.

The thermal stability and decomposition behaviour of MIL-101(Al)–$NH_2$ and hypericin-loaded material were investigated using thermogravimetric analysis (TG) and differential scanning calorimetry (DSC), as presented in Fig. 2C and D, respectively. The TG curves indicate a multi-step mass loss for both samples. For MIL-101(Al)–$NH_2$, the initial weight loss (8.21 wt%) observed below 200 °C is attributed to the removal of adsorbed water and residual organic solvent molecules from the framework. A second significant weight loss (46.2 wt%) occurs between 350 °C and 600 °C, corresponding to the decomposition of the organic linker, 2-aminoterephthalate ligand. In contrast, the hypericin-loaded sample, MIL-101(Al)–$NH_2$ Hyp, exhibits a similar initial weight loss (7.65 wt%) up to 200 °C, which is also related to solvent removal. However, a slightly higher mass loss (46.72 wt%) is observed in the second stage, likely due to the decomposition of both the organic linker and the incorporated hypericin molecules, indicating a change in thermal stability because of the loading process. The DSC curves further support the mentioned observations. On the DSC curve of MIL-101(Al)–$NH_2$, an exothermic peak with a maximum is evident at 481 °C, associated with the decomposition of the linker. In the case of MIL-101(Al)–$NH_2$ Hyp, the exothermic peak shifts slightly to 502 °C and appears more intense, reflecting the additional degradation heat processes associated with hypericin decomposition.

The nitrogen adsorption/desorption isotherms of MIL-101(Al)–$NH_2$ and hypericin-loaded MIL-101(Al)–$NH_2$ measured at −196 °C are presented in Fig. 2E, providing insights into the surface area, pore volume, and porosity changes induced by hypericin loading. Both materials exhibit type *IV* isotherms, characteristic of mesoporous materials, with a hysteresis loop indicating capillary condensation in the mesopores [67]. For MIL-101(Al)–$NH_2$, the Brunauer–Emmett–Teller surface area ($S_{BET}$) is 1568 $m^2\ g^{-1}$, and the total pore volume ($V_p$) is 0.918 $cm^3\ g^{-1}$. After loading with hypericin, the surface area and pore volume decrease slightly to 1498 $m^2\ g^{-1}$ and 0.902 $cm^3\ g^{-1}$, respectively. The observed reduction in BET surface area and pore volume confirms the successful incorporation of hypericin within the pores of MIL-101(Al)–$NH_2$. The isotherm profiles for both samples remain similar, indicating that the structural framework of the material is preserved after hypericin loading. However, the slight reduction in the adsorbed nitrogen volume at higher relative pressures ($p/p_0$) for MIL-101(Al)–$NH_2$ Hyp further supports the partial pore blockage or occupation by hypericin molecules [68].

The release profile of hypericin from the MIL-101(Al)–$NH_2$ matrix is depicted in Fig. 2F. The release behaviour occurs in two distinct phases. In the initial phase, during the first hour (with time intervals of 0.25; 0.5; and 1 h), the release of hypericin into PBS media is relatively slow, attributed to its poor solubility in water. During this period, only 3.26 % of hypericin is released. Following the addition of a 10 % FBS solution, a significant enhancement in hypericin release is observed due to increased solubility facilitated by its monomerisation. After 4 h, 58.51 % of the total hypericin is released. The release continues progressively, reaching 99.38 % after 24 h, indicating an almost complete release of hypericin into the media. This two-step release profile highlights the role of FBS in modulating the solubility and subsequent release of hypericin [31].

As part of this study, the stability of MIL-101(Al)–$NH_2$ was evaluated after immersion in dimethyl sulfoxide (DMSO), phosphate-buffered saline (PBS), and fetal bovine serum (FBS) at 37 °C for 48 h. A combination of IR spectroscopy, PXRD, and SEM with EDX was used to assess structural changes, elemental composition, and particle size distribution.

PXRD analysis (Fig. S2A in ESI) revealed a decrease in peak intensity for all samples compared to the pristine material. For the samples impregnated with PBS and FBS, several diffraction peaks in the 15–20° $2\theta$ range were missing compared to the calculated XRD pattern. This suggests that the polycrystalline form of MIL-101(Al)–$NH_2$ was partially transformed into a semi-amorphous state [69], consistent with findings reported in [70]. This transformation was further confirmed by infrared spectroscopy (Fig. S2B in ESI). The spectra of the treated samples were similar to that of the pristine material, except for the appearance of a new absorption band at 1068 $cm^{-1}$, corresponding to the stretching $\nu$(P—O) vibration of phosphates from PBS and FBS solutions. In the sample treated with DMSO, a new absorption band appeared at 1006 $cm^{-1}$, attributed to the stretching $\nu$(S—O) vibration from DMSO. Fig. S3 in ESI provides a comparative visualization of the material's morphology and chemical composition before and after exposure to different media. The SEM image of the synthesized MIL-101(Al)–$NH_2$ (Fig. S3A in ESI) reveals an aggregated particle morphology with a highly textured and porous structure. While distinct octahedral crystallites are not clearly discernible, likely due to particle agglomeration and surface roughness, the observed features suggest a hierarchical assembly of primary nanocrystals. Elemental analysis via EDX spectroscopy (Fig. S3B in ESI) and elemental mapping (Fig. S3C in ESI) confirm the presence of the expected elements (C, O, N, and Al) consistent with the material's composition. Additionally, particle size distribution analysis derived from SEM imaging indicates that the majority of particles are below 100 nm in size (Fig. S3D in ESI). Further SEM analysis was conducted on samples exposed to different media for 48 h. The DMSO-treated sample (Fig. S3E in ESI) appears to enhance the purity of the pristine material. In contrast, samples treated with PBS and FBS (Figs. S3F and G in ESI) exhibit slight surface roughening of their polycrystalline structure, transitioning toward a semi-amorphous state, likely due to the adsorption of phosphate and fetal bovine serum components onto the nanoparticles. The presence of phosphates was further confirmed by EDX analysis, as evidenced by the detection of phosphorus in the treated samples (see Figs. S3H and I in ESI).

### 3.2. Spectroscopic properties of MIL-101(Al)–$NH_2$ and its suitability for in vivo bioimaging

The fluorescence properties of MIL-101(Al)–$NH_2$ particles were

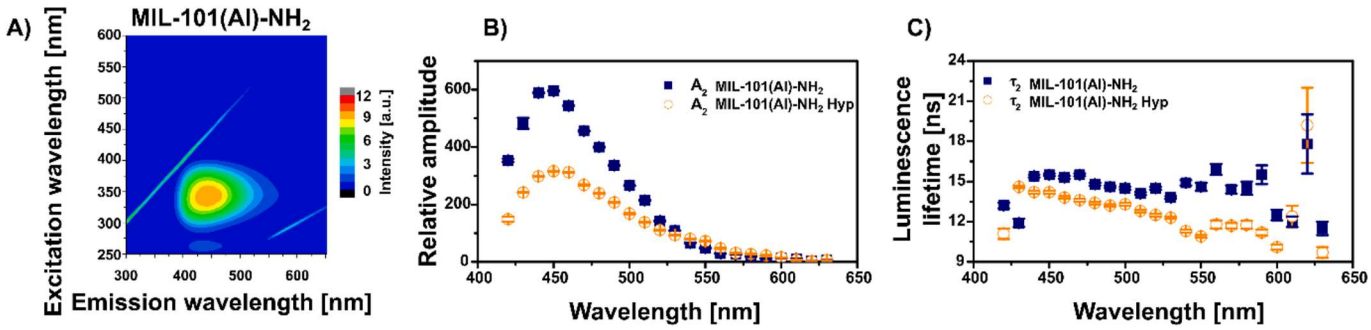


**Fig. 3.** (A) Excitation and emission matrix of 0.02 mg/mL MIL-101(Al)–$NH_2$ in the aqueous solutions. (B) Amplitudes ($A_2$) and (C) fluorescence lifetimes ($\tau_2$) determined from the decay of the fluorescence of MIL-101(Al)–$NH_2$ (blue square) and MIL-101(Al)–$NH_2$ loaded with hypericin (orange circles) in the spectral range from 420 nm to 630 nm. The samples were stimulated with a 405-pulsed LED. The bi-exponential analysis was performed on the detected fluorescence decays to determine the parameters. (For interpretation of the references to colour in this figure legend, the reader is referred to the web version of this article.)

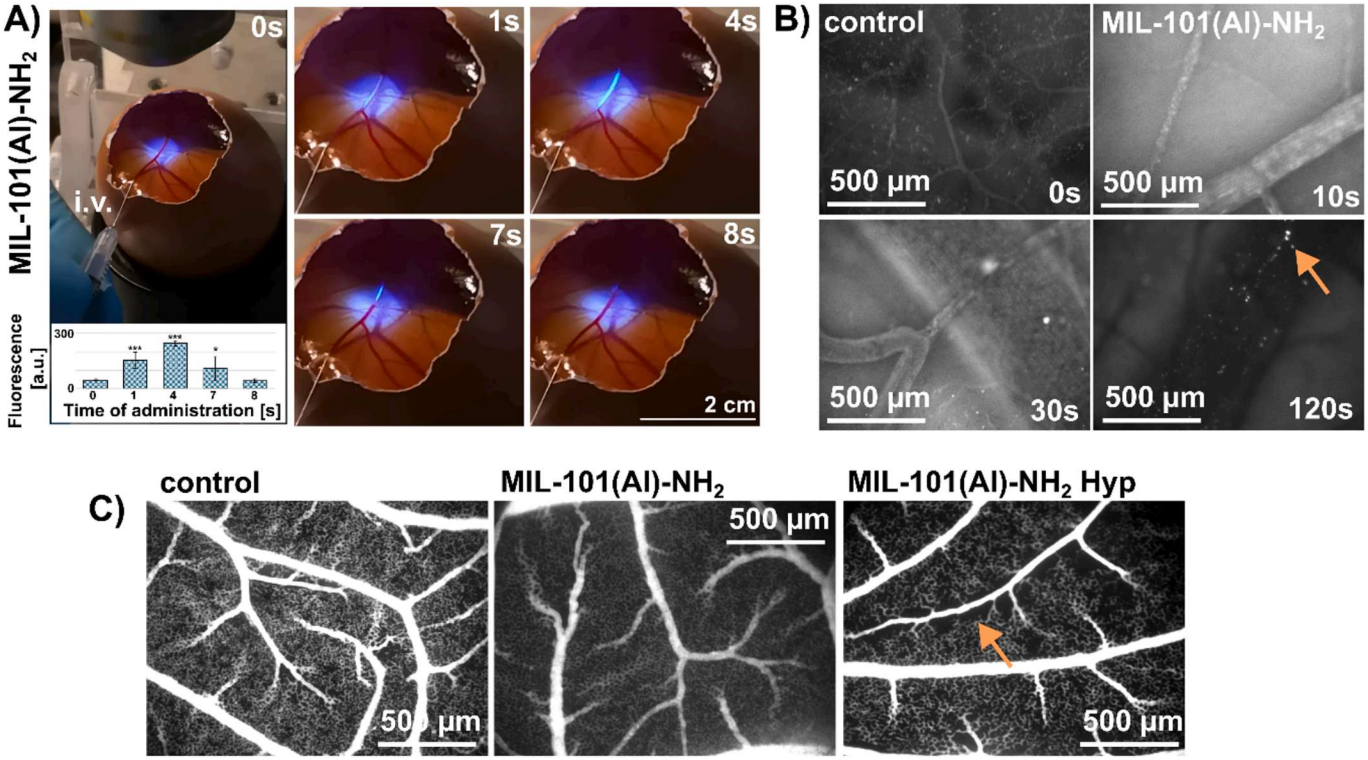


**Fig. 4.** (A) Intravenous (i.v.) administration of 50 μL of 2 mg/mL MIL-101(Al)–$NH_2$ a in the CAM model. MIL-101(Al)–$NH_2$ particles are visible as bright cyan fluorescence 1, 4, 7 and 8 s after administration. The averaged fluorescence intensities were plotted in the histogram (statistical significance: *$p < 0.05$, ***$p < 0.001$). The fluorescence was stimulated with light from the microscope in the UV range (excitation 365/10, emission filtered by DM400 and BA410). (B) Intravascular and extravascular biodistribution of MIL-101(Al)–$NH_2$ during 120 s after their intravenous administration. The orange arrow indicates bright foci of MIL-101(Al)–$NH_2$ particles in the main vein. (C) Angiographies of CAM vessels highlighted with dextran-FITC. Images were taken 24 h after intravenous administration of MIL-101(Al)–$NH_2$ and MIL-101(Al)–$NH_2$ Hyp. The orange arrow indicates inhibition of capillary growth. (For interpretation of the references to colour in this figure legend, the reader is referred to the web version of this article.)

investigated with the aim of identifying their potential for fluorescent bioimaging. Representative absorption and fluorescence spectra of hypericin can be found in Fig. S4 in the supplementary material. The main absorption of hypericin is at 600 nm with a second maximum at 560 nm (black spectrum). The fluorescence spectrum is a mirror image of the absorption with a maximum at 600 nm (red spectrum). This fluorescence does not significantly interfere with the emission of MIL-101(Al)–$NH_2$, but the absorption of hypericin in the UV and blue range enables an energy transfer from the particles to hypericin. Due to this transfer, the emission of the particles and the corresponding lifetime can serve as an indicator of hypericin loading in the particles and subsequent release into the biological environment [71,72].

Excitation and emission matrices of MIL-101(Al)–$NH_2$ in the absence and presence of hypericin are shown in Fig. 3A and B. Bright emissions were observed at excitation maxima between 300 and 400 nm, which is consistent with the observations of Lin and coworkers [73]. The luminescence intensity of MIL-101(Al)–$NH_2$ decreased in the presence of hypericin. This indicates that hypericin can be incorporated into the particles. Time-resolved measurements of the fluorescence lifetime of MIL-101(Al)–$NH_2$ can confirm this hypothesis.

The lifetime of fluorescence luminescence is an interesting parameter that describes the local environment of the fluorescent molecules [74]. The NanoLED source at 405 nm was used to determine the luminescence lifetime of MIL-101(Al)–$NH_2$ at different emission

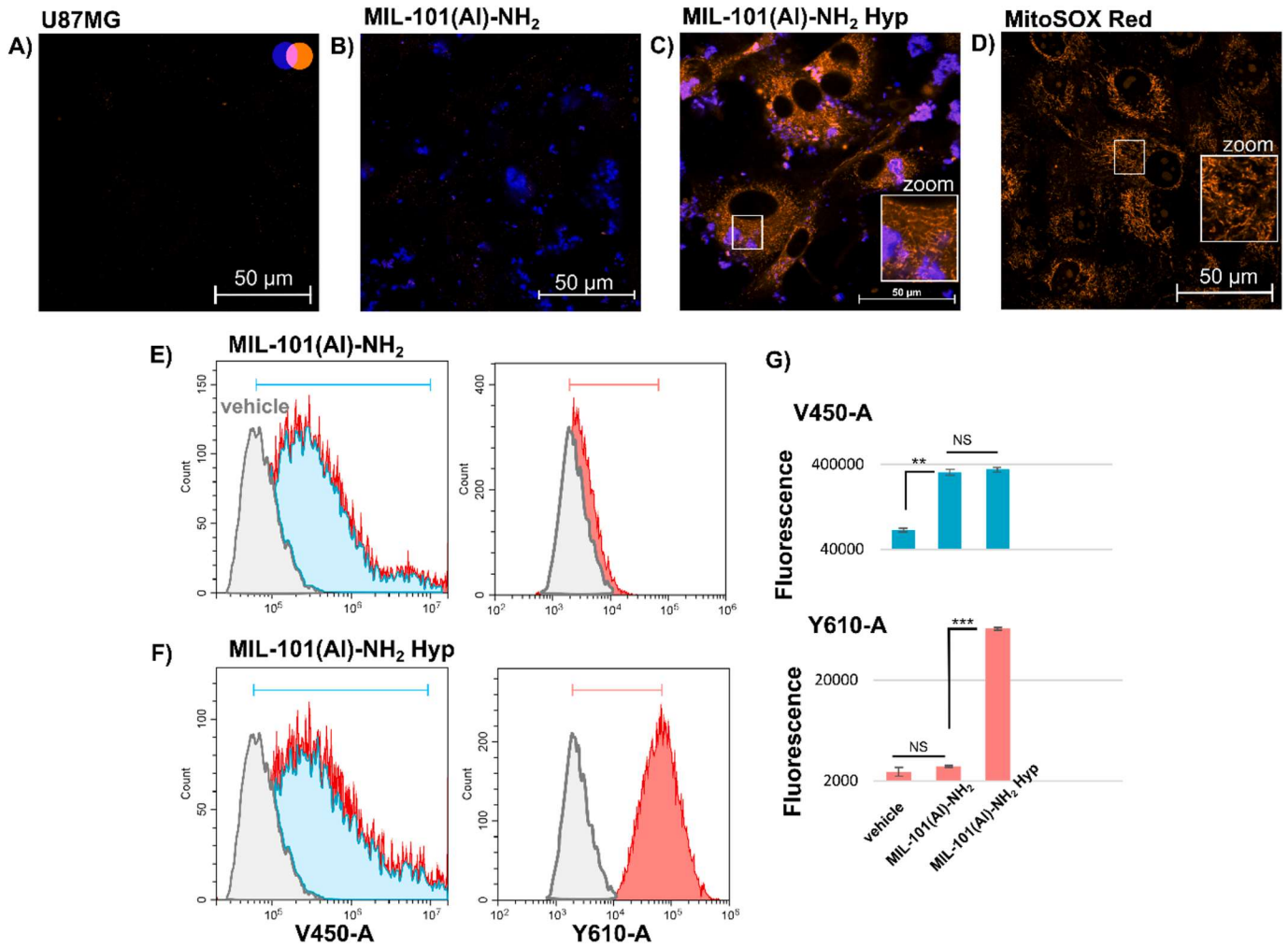


**Fig. 5.** Fluorescence images of (A) U87MG cells exposed to (B) 0.2 mg/mL MIL-101(Al)–$NH_2$ and (C) 0.2 mg/mL MIL-101(Al)–$NH_2$ Hyp for 24 h (particles in blue, hypericin in orange). (D) Representative fluorescence image of U87MG cells labelled with MitoSOX Red, a sensor for mitochondrial superoxide. (E, F) Flow cytometric distribution histograms of particles (V450-A, blue marker) and hypericin (Y610-A, red marker) fluorescence in U87MG cells. The red marker in E serves only to illustrate the maximum of hypericin fluorescence intensity. (G) Averaged fluorescence intensities detected in the V450-A and Y610-A channels. The error bars represent standard deviations from the average values ($n = 3$). The level of significant difference was estimated using a one-way ANOVA test: *$p < 0.05$, **$p < 0.01$, and ***$p < 0.001$, NS-not significant. (For interpretation of the references to colour in this figure legend, the reader is referred to the web version of this article.)

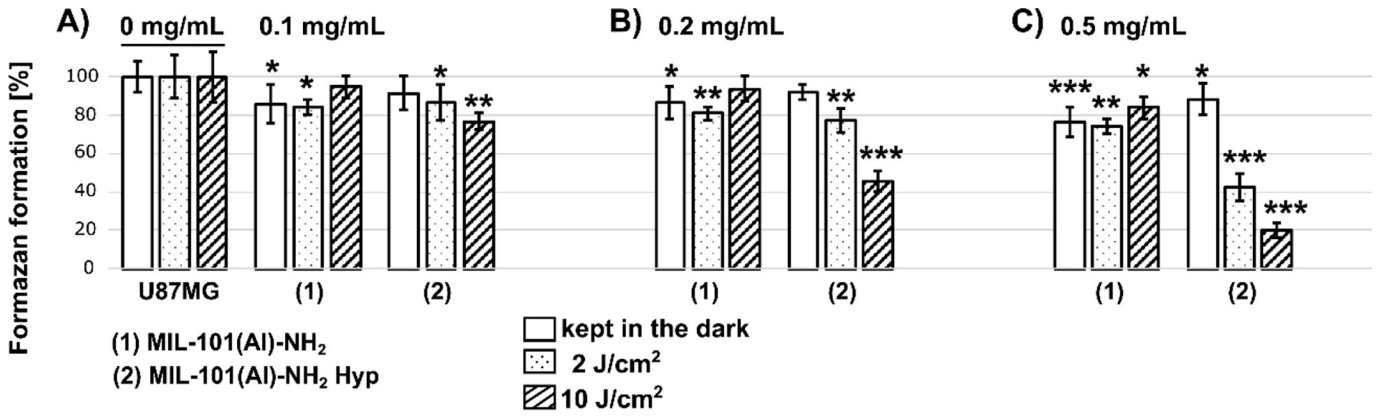


**Fig. 6.** Phototoxicity assessment with MTT-assay of formazan formation in U87MG cells treated with (A) 0.1, (B) 0.2 and (C) 0.5 mg/mL of MIL-101(Al)–$NH_2$ and MIL-101(Al)–$NH_2$ Hyp for 24 h in the dark (white columns) and exposed to 590 nm diode light (3 h after administration of particles) with light doses 2 and 10 J/$cm^2$ as denoted in graph. A one-way ANOVA test was used to determine the level of significant difference between control (indicated as 0 mg/mL) and treated cells: *$p < 0.05$, **$p < 0.01$, and ***$p < 0.001$.

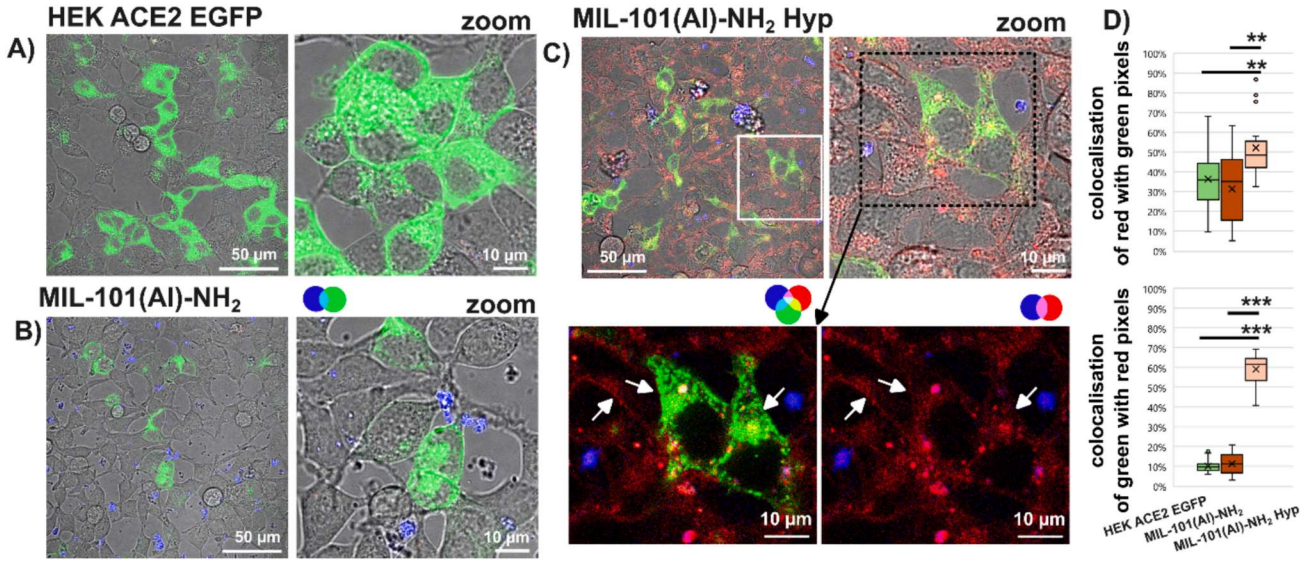


**Fig. 7.** (A) Expression of EGFP-labelled ACE2r in HEK cells (green). Cells were incubated for 24 h with (B) 0.2 mg/mL MIL-101(Al)–$NH_2$ and (C) 0.2 mg/mL MIL-101(Al)–$NH_2$ Hyp particles. Live cell images were recorded in brightfield and fluorescence mode. MIL-101(Al)–$NH_2$ particles are shown in blue, and hypericin in red. The mixing of colours during colocalisation analysis is shown by colour-coded circles. White arrows indicate the hypericin-loaded plasma membrane. (D) Colocalisation efficiency (defined by Manders' coefficients) of red at the place of green pixels, and green at the place of red pixels in corresponding images ($n = 20$ EGFP-labelled cells). The level of significant difference was determined using an one-way ANOVA test: **$p < 0.01$, ***$p < 0.001$. (For interpretation of the references to colour in this figure legend, the reader is referred to the web version of this article.)

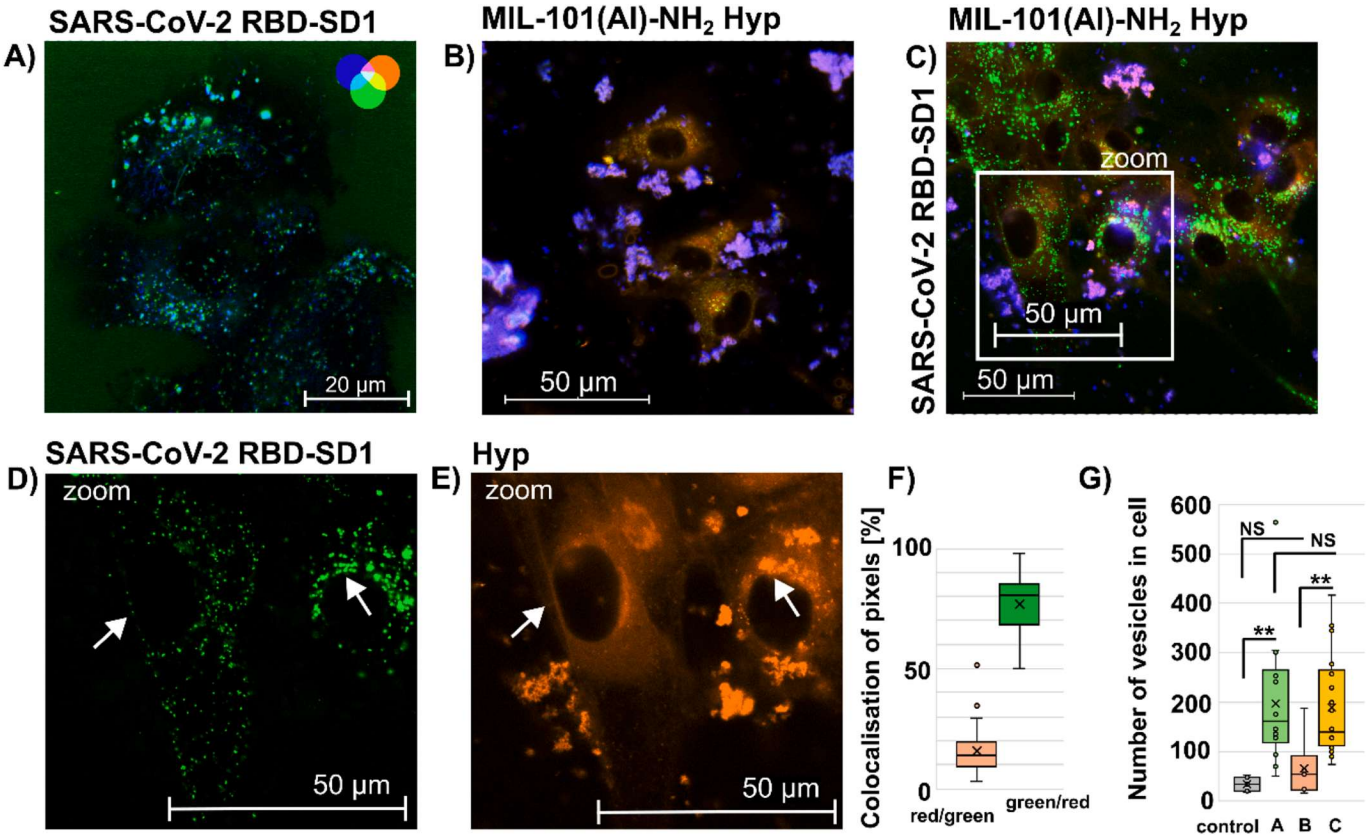


**Fig. 8.** (A) Fluorescence images of U87MG cells exposed to 0.02 mg/mL SARS-CoV-2 RBD-SD1 conjugated with AlexaFluor 488 (green) for 24 h. (B) Cells exposed to 0.2 mg/mL MIL-101(Al)–$NH_2$ Hyp for 3 h. Hypericin fluorescence is shown in orange, and particles in blue. (C) Cells exposed to SARS-CoV-2 RBD-SD1 conjugated with AlexaFluor 488 (24 h) and MIL-101(Al)–$NH_2$ Hyp (3 h). The zoom image was split into (D) green and (E) orange channels. White arrows indicate the localisation of SARS-CoV-2 RBD-SD1-loaded vesicles in the cells. (F) Colocalisation of red with green, and green with red pixels determined from C ($n = 36$ images). G) The number of vesicles detected in the green channel was determined from untreated control and cells exposed to treatments presented in A–C. One-way ANOVA was used to determine the level of significant differences between treatments: **$p < 0.01$, NS – not significant. (For interpretation of the references to colour in this figure legend, the reader is referred to the web version of this article.)

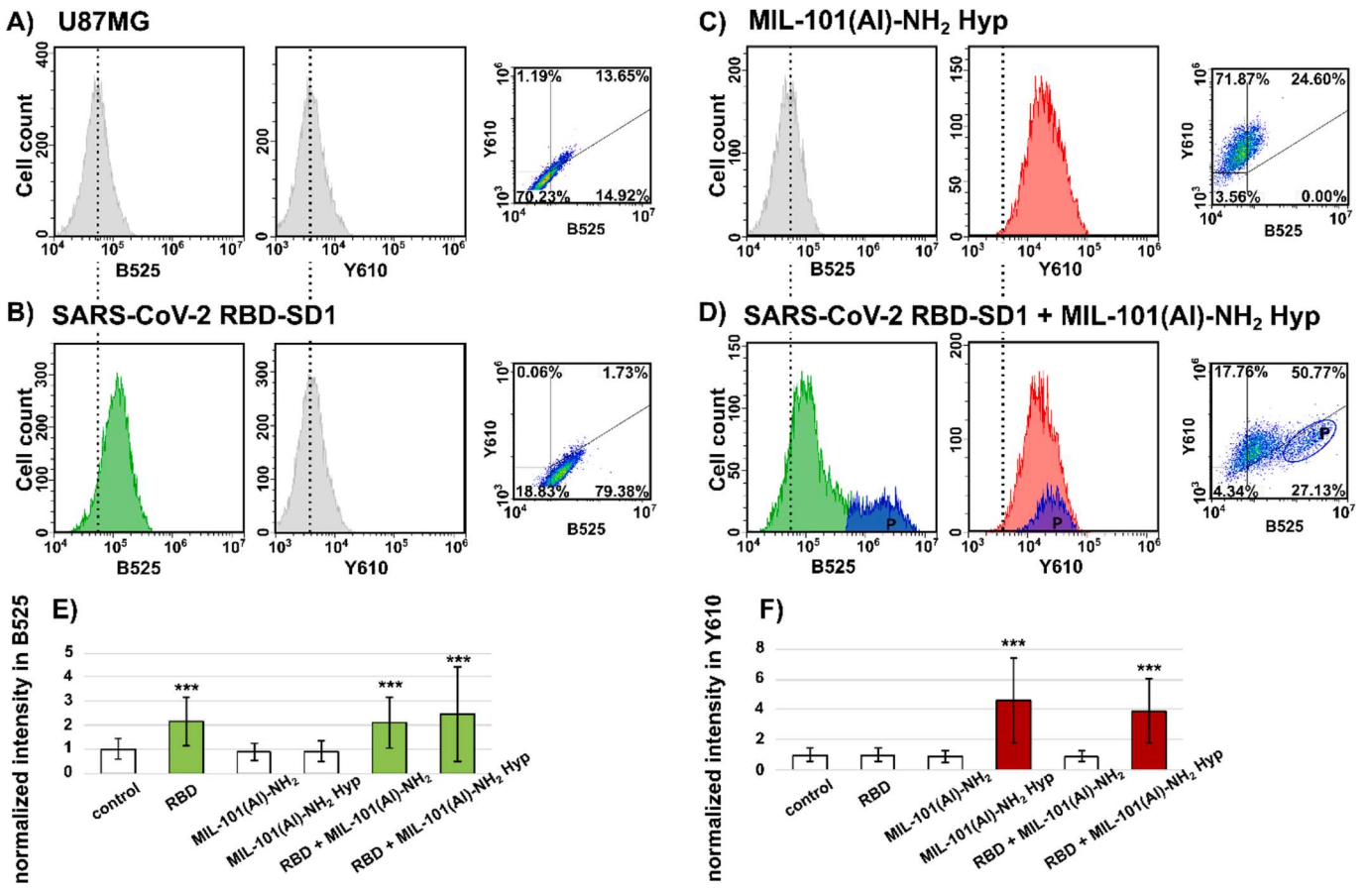


**Fig. 9.** Flow cytometric analysis of (A) U87MG cells in the presence of (B) 0.02 mg/mL SARS-CoV-2 RBD-SD1 conjugated with AlexaFluor 488 (green), (C) 0.2 mg/mL MIL-101(Al)–$NH_2$ Hyp (red) and (D) a combination of both. The correlation diagram of the B525 and Y610 intensities can be found in the insert. The new population in the B525 channel was identified as P and was also recognised in the Y610 channel. Statistical analysis of fluorescence intensities (in triplicate) in (E) B525 channel and (F) Y610 channel. An one-way ANOVA test was performed to determine the level of significant differences from the control: ***$p < 0.001$. (For interpretation of the references to colour in this figure legend, the reader is referred to the web version of this article.)

wavelengths. The 3D luminescence decays are shown in the supplementary materials in Fig. S5C and D for both MIL-101(Al)–$NH_2$ in the absence and presence of hypericin. The parameters of the amplitudes and components of the luminescence lifetimes were derived from bi-exponential fits of the decays (see Fig. S5, Table S1 and Table S2 in the supplementary material). Longer lifetimes $\tau_2$, and corresponding amplitudes $A_2$ were plotted in Fig. 5B and C. A significant decrease in amplitudes was observed in the presence of hypericin in the spectral range between 420–525 nm (Fig. 3B). On the other hand, a decrease in luminescence lifetime was observed with the maximum difference in the spectral range between 525–600 nm (Fig. 3C), a major absorption of hypericin. This confirms the incorporation of hypericin into MIL-101(Al)–$NH_2$. Furthermore, these spectral parameters (excitation between 300–400 nm and emission 450–500 nm) may define the optical window for successful *in vivo* imaging of MIL-101(Al)–$NH_2$.

The microvasculature system developed in the CAM was used in this study to validate the suitability of MIL-101(Al)–$NH_2$ for *in vivo* bioimaging and 24 h biocompatibility. CAM is a reliable model commonly used for preclinical drug screening, photodiagnostics and phototoxicity assessment [75–77].

As previously mentioned, bioimaging of MIL-101(Al)–$NH_2$ was performed in real-time using an epifluorescence microscope at 360–370 nm excitation after intravenous (i.v.) administration of 50 μL MIL-101(Al)–$NH_2$ in physiological solution (Fig. 4A). During administration, a bright blue luminescence can be observed in white light. However, this luminescence disappeared shortly after administration, probably due to the systemic distribution of the particles in the bloodstream. Microscopic images of CAM vessels were obtained by filtering the emission with a combination of DM400 and BA410 filters (Fig. 4B).

Bright luminescence was detected in the CAM vessels and capillaries up to 30 s after administration. The bright foci of MIL-101(Al)–$NH_2$ were identified in the walls of the large vessels (>500 μm) in later seconds (see orange arrow in Fig. 4B).

The acute toxicity of the particles was investigated 24 h after i.v. administration. All tested embryos ($n = 4$ per case) survived, indicating a certain biocompatibility of MIL-101(Al)–$NH_2$ and MIL-101(Al)–$NH_2$ Hyp, as carriers.

Hypericin is known for its minimal dark toxicity [17]. However, its inhibitory effect on cell signalling during proliferation, which is mainly related to protein kinase C, has been observed [78–80]. Lavie et al. reported the inhibitory effect of hypericin on neovascularisation in ophthalmology [81], and the antiangiogenic effect of hypericin was also suggested by Martinez-Poveda et al. in the study of endothelial cell proliferation, migration and invasion [82].

The fluorescence angiographies of CAM recorded after contrasting with dextran-FITC and black ink are shown in Fig. 4C. Occlusion of small capillaries (>10 μm) was observed in CAMs treated with MIL-101(Al)–$NH_2$ Hyp (see orange arrow in Fig. 4C). It should be noted that the CAMs were kept in the dark for 24 h after administration. While MIL-101(Al)–$NH_2$ did not induce any changes in the vasculature, the inhibition of capillary growth can be attributed to the bioactivity of hypericin and the anti-angiogenic effect in the dark.

To determine the dosage of the drug, the toxicity of MIL-101(Al)–$NH_2$ and MIL-101(Al)–$NH_2$ Hyp in the dark was investigated in human

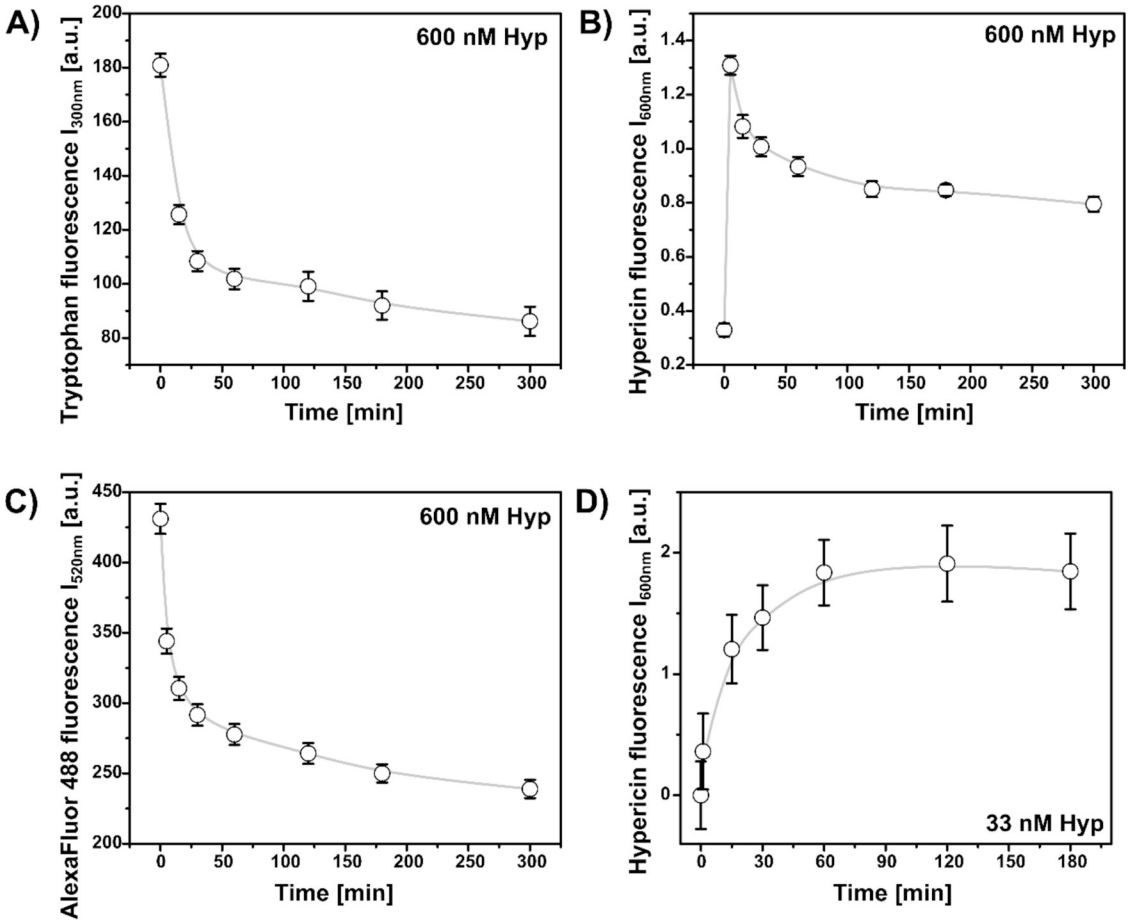


**Fig. 10.** Interaction of 0.0017 mg/mL SARS-CoV-2 RBD-SD1 (RBD) with hypericin. (A) Fluorescence of RBD tryptophan in the presence of 600 nM hypericin for 300 min. (B) Fluorescence of 600 nM hypericin in the presence of RBD for 300 min. (C) Fluorescence of 0.0013 mg/mL AlexaFluor 488 in RBD-A488 in the presence of 600 nM hypericin for 300 min. (D) Fluorescence of 33 nM hypericin in the presence of RBD.

dermal fibroblasts (HDF) for 48 h. The results of the MTT-assay in terms of metabolic activity of the cells are shown in Fig. S6 of the supplementary material. While an $IC_{50}$ value of 0.15 mg/mL was found for MIL-101(Al)–$NH_2$, a higher $IC_{50}$ value of 0.25 mg/mL was found for MIL-101(Al)–$NH_2$ Hyp. It should be noted that this cell line represents healthy tissue cells, which have a slow proliferation rate compared with cancer cells. It is to be expected that too high a concentration of particles applied topically to the tissue may lead to local irritation of this tissue as a confluent layer forms on the surface, as observed in our previous work for mesoporous materials [37,83]. The results of the MTT-assay indicate that hypericin can reduce the toxicity caused by MIL-101(Al)–$NH_2$ in the dark and thus significantly influence the biocompatibility of the particles.

Considering the different functionalities and modularity of MOFs, the multimodality of such a system can provide the structural information *in vivo* using advanced imaging techniques such as magnetic resonance imaging, computed tomography, ultrasound and other optical techniques that provide functional and molecular information [84].

### *3.3. Subcellular distribution of hypericin transported into cells by MIL-101(Al)–$NH_2$ and its photodynamic activity*

The modification of MIL-101 particles and the incorporation of photocatalysts or photosensitisers can lead to an improvement in their photosensitisation and bioavailability [85–87]. However, the transport into the cells depends on the size of the MOF particles [88]. Particles smaller than 150 nm can be transported into the cell *via* endocytosis, which is also the favoured route for various macromolecules and viruses, including SARS-CoV-2 [4].

Here, the particle size was chosen so that a large number of hypericin molecules can enter the cells while the particles adhere to the cell surface. The MIL-101(Al)–$NH_2$ Hyp particles were therefore applied to U87MG cells to determine the uptake rate of hypericin and subsequently to determine its subcellular distribution in HEK cells expressing higher numbers of ACE2r.

The distribution of particles and hypericin in the presence of U87MG cells is shown in Fig. 5B and C. MIL-101(Al)–$NH_2$ (blue colour) is localised in the extracellular space and only some of them adhere to the surface and inside the cells (smaller particles). Hypericin fluorescence (orange and pink) was identified inside the particles and in the cells with bright localisation in tubular structures (Fig. 5C). These structures were identified as mitochondria using the MitoSOX Red fluorescence probe (Fig. 5D).

The uptake of particles and hypericin was analysed by flow cytometry (Fig. 5E-G). MIL-101(Al)–$NH_2$ was positively identified in the V450 channel at 405 nm excitation. Hypericin was detected in the Y610 channel at 561 nm and only when MIL-101(Al)–$NH_2$ Hyp was applied (Fig. 5F and 5G). These results confirm the internalisation of hypericin in U87MG cells. Furthermore, mitochondrial localisation indicates an important role of hypericin in apoptosis of these cells, especially after PDT.

The efficacy of PDT, which is triggered by hypericin transported in MIL-101(Al)–$NH_2$, was found to be concentration- and light dose-dependent. The metabolic activity of U87MG cells was slightly impaired by the particles in the dark and in the absence of hypericin (Fig. 6). However, a significant decrease in metabolic activity (below 60

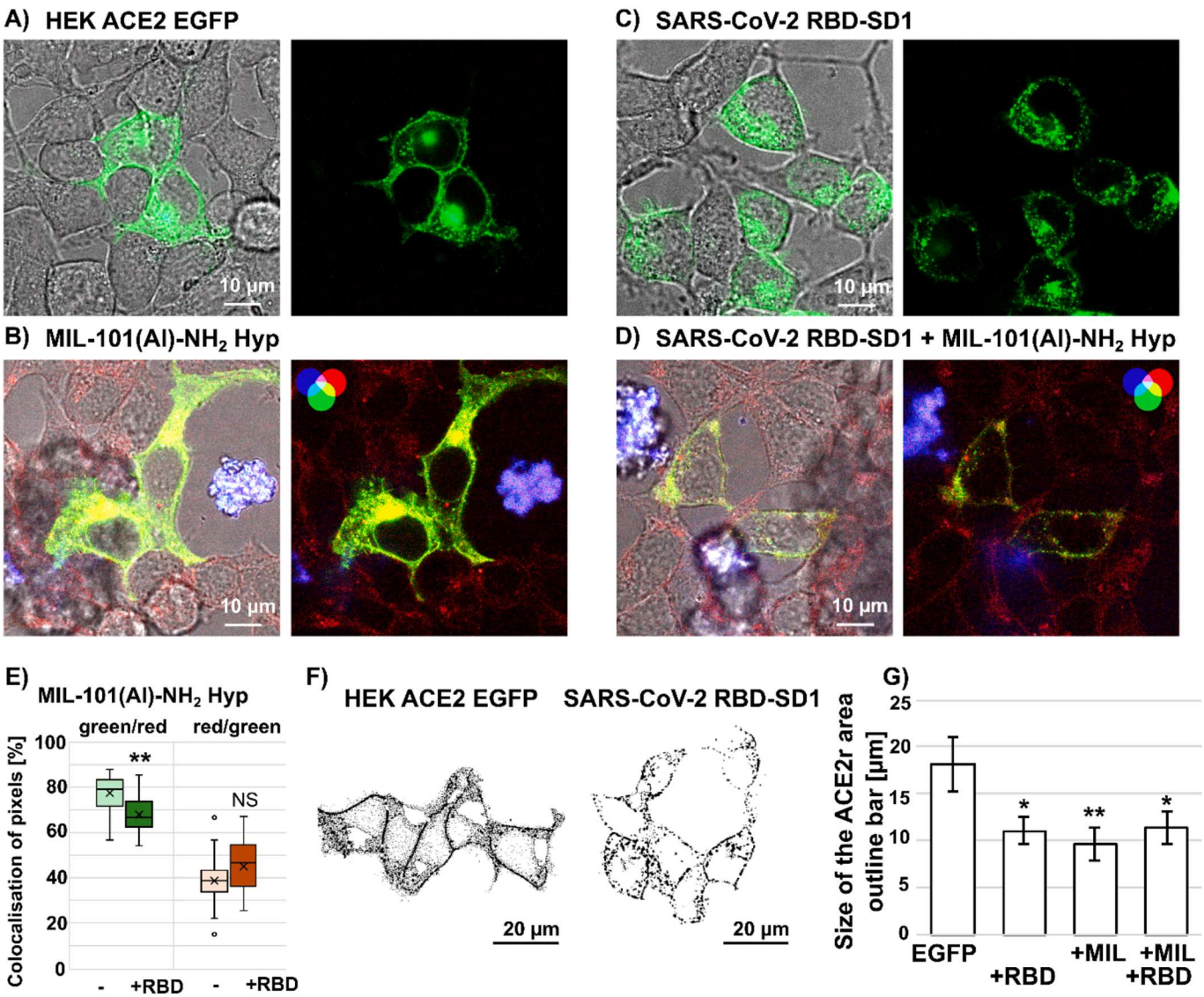


**Fig. 11.** Overlapped brightfield and fluorescence images of (A) HEK ACE2 EGFP cells in the absence and (B) in the presence of 0.2 mg/mL MIL-101(Al)–$NH_2$ Hyp, (C) 0.025 mg/mL SARS-CoV-2 RBD-SD1 and (D) a combination of both for 5 h. EGFP is shown in green, hypericin in red and particles in blue. (E) Red and green pixel colocalisation derived from colocalisation analysis of B and D cases. (F) Representative images of EGFP obtained after threshold adjustment in cells without and with RBD administration. (G) The size of ACE2r area outline bar is determined from threshold images. An one-way ANOVA test was performed to determine the level of significant differences from the control (without RBD): *$p < 0.05$, **$p < 0.01$. (For interpretation of the references to colour in this figure legend, the reader is referred to the web version of this article.)

%) was observed after the cells (MIL-101(Al)–$NH_2$ Hyp) were irradiated with 2 and 10 J/$cm^2$. The higher the concentration, the stronger the effect (Fig. 6C). These results indicate the availability of MIL-101(Al)–$NH_2$ Hyp for PDT.

It has been reported that SARS-CoV-2 mainly affects cells with a high expression of ACE2r [2]. Therefore, we tested the ability of MIL-101(Al)–$NH_2$ to transport hypericin into cells expressing ACE2r. Fig. 7 shows HEK cells with high (green EGFP-labelled cells) and low ACE2r expression. Note that EGFP was expressed both in the plasma membrane (localisation of ACE2r) and in the cytoplasm of the cells (Fig. 7A). The MIL-101(Al)–$NH_2$ particles were localised near the cell surface, similar to the case of U87MG (Fig. 7B). The MIL-101(Al)–$NH_2$ Hyp particles were applied to these cells for 24 h. Fig. 7C shows that hypericin was internalised by both cell types. Hypericin was found in punctate foci within the cells and in the plasma membranes (see white arrows in Fig. 7C). Interestingly, punctate localisation of EGFP was observed in cells with high ACE2r exposed to hypericin. Significantly higher colocalisation of hypericin and EGFP was observed in cells exposed to MIL-101(Al)–$NH_2$ Hyp (Fig. 7D). This suggests that hypericin is present in the vesicles and membranes containing ACE2r. Wang and coworkers have shown that SARS-CoV-2 can enter cells together with ACE2r by endocytosis [89]. It can be assumed that hypericin enforces endocytosis of the receptors, but a detailed analysis should be carried out in a follow-up study.

### *3.4. Intracellular localisation of SARS-CoV-2 RBD-SD1 and its interaction with MIL-101(Al)–$NH_2$ Hyp*

Endocytosis is not only the mechanism by which the particles enter the cells, but also the route by which SARS-CoV-2 RBD-SD1 can infect the cells. To test this hypothesis, U87MG cells expressing low levels of ACE2r [90] were exposed to SARS-CoV-2 RBD-SD1 labelled with AlexaFluor488 (RBD-A488). After 24 h, numerous vesicles loaded with RBD-A488 were identified in the cells (Fig. 8A). However, the excess of this protein was located in the extracellular space. These vesicles were not seen in cells lacking RBD-A488 (Fig. 8B). Furthermore, MIL-101(Al)–

**Table 1**
FLIM analysis of EGFP fluorescence lifetime in HEK ACE2 EGFP cells.

| | Amplitude $A_1$ | Component $\tau_1$ (ns) | Amplitude $A_2$ | Component $\tau_2$ (ns) | Average $\tau$ (ns) |
|---|---|---|---|---|---|
| HEK ACE2 EGFP | 0.31 ± 0.23 | 1.30 ± 0.40 | 1.3 ± 0.3 | 2.50 ± 0.10 | 2.30 ± 0.02 |
| HEK ACE2 EGFP + MIL-101 (Al)–$NH_2$ Hyp | 4.00 ± 0.40 | 1.53 ± 0.08 | 8.0 ± 0.4 | 2.66 ± 0.03 | 2.28 ± 0.01 |
| HEK ACE2 EGFP + RBD | 0.97 ± 0.07 | 1.20 ± 0.12 | 2.5 ± 0.3 | 2.62 ± 0.03 | 2.20 ± 0.02 |
| HEK ACE2 EGFP + RBD + MIL-101 (Al)–$NH_2$ Hyp | 0.27 ± 0.16 | 1.40 ± 0.40 | 0.8 ± 0.2 | 2.60 ± 0.10 | 2.29 ± 0.04 |

$NH_2$ Hyp particles were administered to the cells treated with RBD-A488. Similar to Fig. 8A, a large number of green vesicles corresponding to RBD-A488 were clearly visible (Fig. 8C and D). A significant increase in vesicles in cells exposed to RBD-A488 was confirmed by image processing and counting of these vesicles (Fig. 8G).

It can be observed that hypericin could easily penetrate into the cells treated with RBD-A488. However, the localisation was slightly different from the case shown in Fig. 5C. The bright fluorescence of hypericin was detected in the plasma membrane and in the perinuclear region of the endomembrane system, as indicated by white arrows (Fig. 8E). Colocalisation of RBD-A488 and hypericin was observed (Fig. 8C–F), indicating the presence of hypericin in close proximity to RBD. Fig. 8F shows that more than 70 % of green pixels (associated with RBD-A488) are colocalised with red pixels (associated with hypericin) in cells exposed to the combination of RBD-A488 and MIL-101(Al)–$NH_2$ Hyp. The amount of RBD-A488 and hypericin in the cells was then determined by flow cytometry.

Uptake of RBD-A488 by U87MG cells was determined by the green fluorescence of AlexaFluor488 (Fig. 9B and E). Hypericin uptake by cells treated with RBD-A488 followed the same trend as in the absence of RBD-A488 (Fig. 9C, D and F). However, an additional population was detected in the B525 channel (Fig. 9D). This population was also found in the Y610 channel. It should be noted that the particles and RBD-A488 in this experiment were mixed and stabilised for 1 h before being administered to the cells. We have previously shown that mesoporous particles can adsorb proteins by forming a protein corona [91]. Therefore, it can be assumed that part of the RBD-A488 was already adsorbed on MIL-101(Al)–$NH_2$ Hyp. This effect is to be expected, as it has been shown that the material MIL-101 is able to remove small molecules, antibiotics and even rare earth materials from the aqueous environment [92–94].

To confirm this assumption, fluorescence microscopy was performed. Fluorescence images of particles in the absence and presence of RBD-A488 are shown in Fig. S7 in the supplementary material. RBD-A488 has a green fluorescence (Fig. S7E), which is concentrated in MIL-101(Al)–$NH_2$ (Fig. S7C) after interaction, but decreases significantly in MIL-101(Al)–$NH_2$ Hyp (Fig. S7D). The determined fluorescence intensities indicate that RBD-A488 is quenched due to its interaction with hypericin.

The interaction of hypericin as a ligand with SARS-CoV-2 was demonstrated using super-resolution stimulated emission depletion microscopy [22]. However, the binding of hypericin to SARS-CoV-2 RBD-SD1 can also be monitored using fluorescence spectroscopy by quenching of tryptophan and A488 conjugated to RBD. The kinetics of SARS-CoV-2 RBD-SD1 tryptophan fluorescence in the presence of 600 nM hypericin is shown in Fig. 10A. After 5 h of stabilisation, a significant decrease in fluorescence intensity was observed. The fluorescence of hypericin in Fig. 10B shows a clear maximum followed by a gradual decrease in intensity. This effect has been frequently observed when hypericin interacts with proteins and lipids by forming aggregates within or on the surface of the macromolecule [72,95–97]. The interaction of hypericin was also confirmed by recording A488 fluorescence in RBD, which decreased with the time of incubation with hypericin (Fig. 10C). However, hypericin fluorescence is highly dependent on the concentration ratio between hypericin and RBD. At a low concentration (33 nM), hypericin was able to dissolve into RBD, as evidenced by the recovery of fluorescence (Fig. 10D). This is an important result because it means that hypericin itself in RBD can be transported into the cells in a biologically active state (fluorescent monomers), which in turn can influence cellular signalling.

Since we have demonstrated that hypericin interacts with RBD and can colocalise in cells, we performed the study of ACE2r in the presence of SARS-CoV-2 RBD-SD1 and particles. The representative localisation of ACE2r in EGFP HEK cells is shown in Fig. 11A. The uninterrupted plasma membrane localisation is clearly visible. As shown above, the intracellular localisation of ACE2r in EGFP HEK cells is slightly increased in the presence of MIL-101(Al)–$NH_2$ Hyp, but the plasma membrane localisation can still be seen (Fig. 11B). Administration of SARS-CoV-2 RBD-SD1 for 5 h induced intracellular foci of ACE2r, and diminished plasma membrane EGFP labelling was visible (Fig. 11C).

The most striking changes were seen in cells incubated with a combination of MIL-101(Al)–$NH_2$ Hyp and SARS-CoV-2 RBD-SD1 (Fig. 11D). Note that MIL-101(Al)–$NH_2$ Hyp and SARS-CoV-2 RBD-SD1 (RBD for simplicity) were stabilised for 1 h prior to administration (to allow binding). A decrease in EGFP fluorescence and plasma membrane localisation was observed. Analysis of colocalisation showed that RBD added to the cells together with MIL-101(Al)–$NH_2$ Hyp significantly reduced the percentage of green pixels colocalised with red (Fig. 11E). No significant difference was observed in the colocalisation of red with green pixels (orange box graphs in Fig. 11E).

Next, the threshold was adjusted to the green channels of EGFP-related images (see representative images in Fig. 11F) to determine the size of ACE2r (EGFP) objects, shown with outline bars. A significant decrease in this size was observed in cells exposed to RBD and MIL-101 (Al)–$NH_2$ Hyp (denoted as MIL in the graph in Fig. 11G). This result supports the observed fragmentation and reduction in EGFP abundance.

Fluorescence lifetime is a useful parameter that reflects fluctuations and changes in the local environment of the fluorescent molecule. For this reason, the fluorescence lifetime of EGFP was determined in HEK ACE2 EGFP cells before and after treatment with SARS-CoV-2 RBD-SD1 and MIL-101(Al)–$NH_2$ Hyp. The average lifetimes are summarised in Table 1.

Two components of EGFP fluorescence lifetime have been identified. The average fluorescence lifetime reached a value of 2.3 ns. However, no significant difference was found between the two cases. This means that the fluorescence lifetime was not shortened by the presence of RBD or hypericin in the cells. Therefore, it can be assumed that the reduction of EGFP fluorescence in the cells after administration of RBD and MIL-101 (Al)–$NH_2$ Hyp is probably due to a reduction of ACE2r.

All these results suggest that hypericin is not only colocalised with SARS-CoV-2 RBD-SD1 but also contributes to endocytosis of the receptor and a possible silencing of ACE2r expression, which may subsequently lead to a reduction in the internalisation of the entire virus.

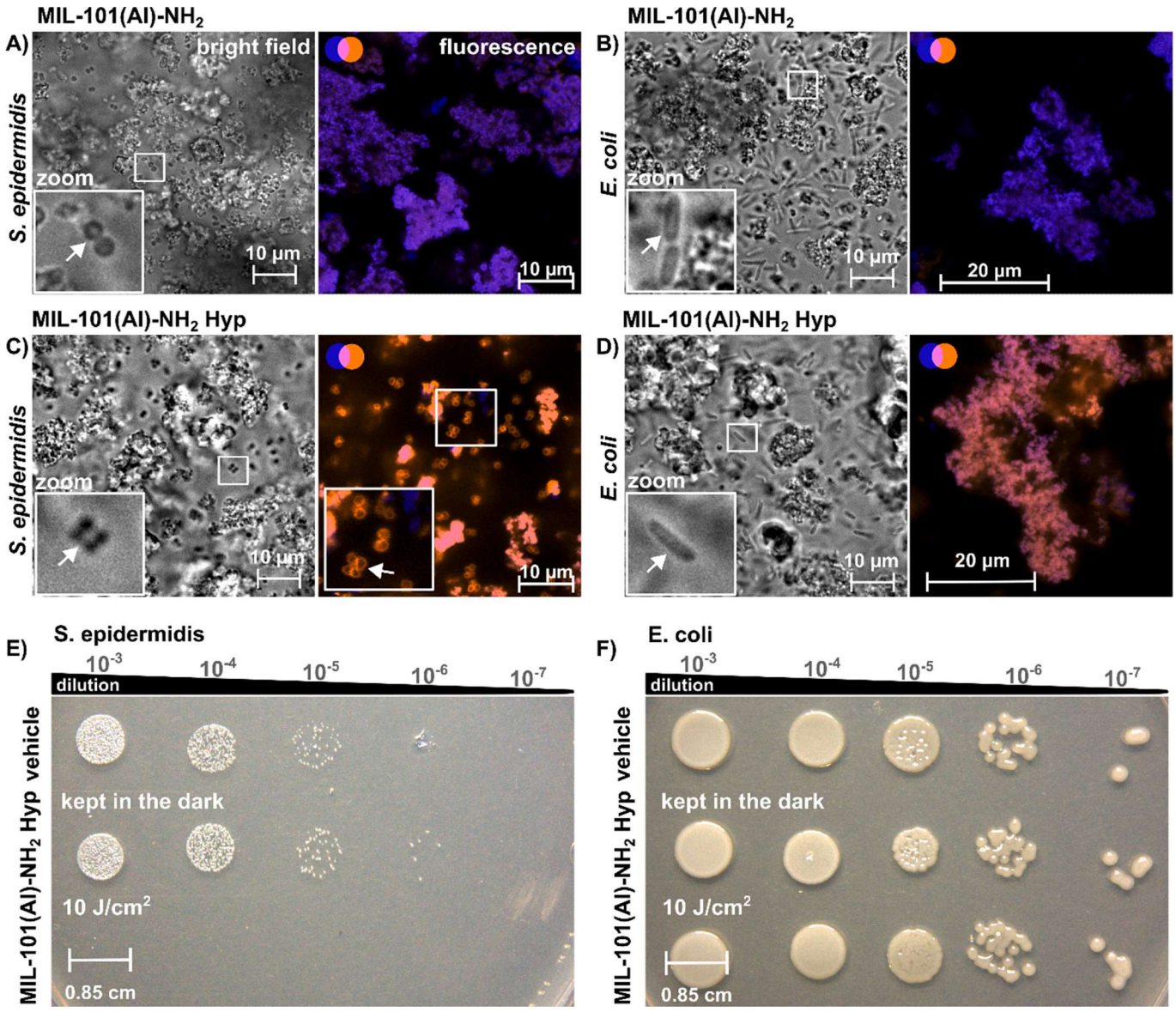


**Fig. 12.** Bright field and fluorescence images of MIL-101(Al)–$NH_2$ incubated with (A) *S. epidermidis* and (B) *E. coli* for 2 h. Hypericin fluorescence (orange colour) contained in MIL-101(Al)–$NH_2$ was detected in (C) *S. epidermidis* and (D) *E. coli* after 2 h of incubation. White arrows indicate bacteria in zoomed images. The viability of the bacteria was evaluated 24 h after inoculation of (E) *S. epidermidis* and (F) *E. coli* exposed to different conditions. The vehicle represents bacterial strains in the absence of the particles. (For interpretation of the references to colour in this figure legend, the reader is referred to the web version of this article.)

### 3.5. Selective photodynamic antibacterial activity of MIL-101(Al) Hyp

Patients with a viral infection are susceptible to secondary bacterial infections. This has also been observed in COVID-19 patients [98]. It was found that the most common bacteria in COVID-19 patients were gram-positive bacteria [99]. Given the increasing resistance of bacteria to antibiotics, it is crucial and one of the risk factors to administer the right antibiotics for treatment [100].

To overcome this problem, photodynamic therapy is on the rise [101,102]. For this reason, the new formulation of MIL-101(Al)–$NH_2$ Hyp was tested on two representative bacterial strains: *S. epidermidis* (gram-positive bacteria) and *E. coli* (gram-negative bacteria).

Bright field and fluorescence images of MIL-101(Al)–$NH_2$ material with *S. epidermidis* and *E. coli* are shown in Fig. 12A and 12B. In the bright field, typically roundish *S. epidermidis* and rod-shaped *E. coli* were identified, but no fluorescence of the bacteria was detected. Blue fluorescence was present in the MIL-101(Al)–$NH_2$ particles. However, administration of MIL-101(Al)–$NH_2$ loaded with hypericin allows identification of the bacteria by fluorescence, as the hypericin is redistributed from the particles into *S. epidermidis*. The orange-coloured bacterial walls are clearly visible in Fig. 12C. This was not observed in *E. coli* (Fig. 12D). This fluorescence shows a certain selectivity of hypericin for gram-positive bacteria.

In addition, the bacterial suspension containing particles was irradiated with 590 nm light to induce PDT with hypericin. The bacteria were then inoculated onto agar at different concentrations for growth. Inhibition of bacterial growth after PDT was only observed for *S. epidermidis* (Fig. 12E). No significant difference was observed in the dark. *E. coli* was not affected by MIL-101(Al)–$NH_2$ Hyp and PDT.

MIL-101 MOFs have recently been identified as an interesting sensor material for the detection of bacteria at low levels [103]. Moreover, upon irradiation with visible and infrared light, the MIL-101(X)–$NH_2$ particles can themselves generate reactive oxygen species and destroy pathogens, depending in the central metal ion (X), enhancing antibacterial and antiviral photodynamic activity [104,105].

The approach presented in this study demonstrates the broad

applicability of the prepared material MIL-101(Al)–$NH_2$ Hyp at the level of proteins, cells and bacteria. While MIL-101(Al)–$NH_2$ was able to adsorb the spike protein and thus reduce its concentration, which could be transported via ACE2r, hypericin loaded into the particles proved to be a promising agent for silencing ACE2r. In addition, hypericin was able to inactivate cells and bacteria by PDT, which could be crucial for reducing secondary infections in patients with viral infections.

## 4. Conclusion

The SARS-CoV-2 pandemic has raised serious concerns about the scientific community's preparedness to combat infectious diseases effectively. It is not only the inactivation of the virus that remains a problem, but also the long-lasting consequences of the disease. Therefore, we have proposed the use of a new combination of hypericin-MOF that could be bioactive at a multimodal level. The interaction of hypericin with the main component of SARS-CoV-2, a spike protein responsible for viral entry into cells, was investigated at the molecular and cellular level. The influence of hypericin and MIL-101(Al)–$NH_2$ on the endocytosis of the spike protein in ACE2r-expressing cells was demonstrated. The photodynamic activity of the construct was demonstrated in cells and bacteria, which adds value to the application of MOFs in this field. The results obtained are promising, but a detailed antiviral activity of the proposed construct should be investigated in further studies.

## CRediT authorship contribution statement

**Veronika Huntošová:** Writing – original draft, Methodology, Investigation, Data curation, Conceptualization. **Anass Benziane:** Writing – original draft, Validation, Investigation, Data curation. **Luboš Zauška:** Writing – original draft, Investigation, Data curation. **Luboš Ambro:** Writing – original draft, Investigation, Data curation. **Soňa Olejárová:** Writing – original draft, Investigation, Data curation. **Jaroslava Joniová:** Writing – original draft, Investigation. **Nina Hlávková:** Investigation. **Georges Wagnières:** Writing – original draft, Investigation. **Gabriela Zelenková:** Writing – original draft, Investigation. **Pavel Diko:** Validation. **Jozef Bednarčík:** Validation. **Florina Zákány:** Investigation. **Tamás Kovács:** Investigation. **Erik Sedlák:** Writing – original draft, Investigation. **György Vámosi:** Writing – original draft, Validation, Conceptualization. **Miroslav Almáši:** Writing – original draft, Investigation, Conceptualization.

## Declaration of competing interest

The authors declare that they have no known competing financial interests or personal relationships that could have appeared to influence the work reported in this paper.

## Acknowledgement

V.H. acknowledge the support funded by the EU NextGenerationEU through the Recovery and Resilience Plan for Slovakia under the project No. 09I03-03-V04-00007. The authors acknowledge Euro-BioImaging (https://www.eurobioimaging.eu) for providing access to imaging technologies and services via the Cellular Imaging Hungary Node (University of Debrecen, Hungary). Part of this work has been funded by the European Union Research and Innovation programme Horizon Europe (ISIDORe – Grant Agreement Number 101046133). GV acknowledges the funding of this research by the National Research, Development and Innovation Office (grants K146028 and ANN 135107). This work was partially supported by the Swiss National Science Foundation (Grant No. IC00I0-232221). M.A. acknowledge the support funded by the Slovak Research and Development Agency under project No. APVV-23-0097 and the Development Operational Programme Integrated Infrastructure for the project "Nanoparticles for solving diagnostic-therapeutic problems with COVID-19 (NANOVIR)", ITMS 2014+: 313011AUW7, co-founded by the European Regional Development Fund (ERDF).The authors also acknowledge Dr. Peter Letovanec and ZEISS company for support with super-resolution microscopy using the Airyscan system.

## Appendix A. Supplementary data

Supplementary data to this article can be found online at https://doi.org/10.1016/j.jcis.2025.137454.

## Data availability

Data will be made available on request.

## References

[1] S. Lopez-Leon, T. Wegman-Ostrosky, C. Perelman, R. Sepulveda, P.A. Rebolledo, A. Cuapio, S. Villapol, More than 50 long-term effects of COVID-19: a systematic review and meta-analysis, Sci. Rep. 11 (2021), https://doi.org/10.1038/s41598-021-95565-8.
[2] J. Shang, G. Ye, K. Shi, Y. Wan, C. Luo, H. Aihara, Q. Geng, A. Auerbach, F. Li, Structural basis of receptor recognition by SARS-CoV-2, Nature 581 (2020), https://doi.org/10.1038/s41586-020-2179-y.
[3] C.B. Jackson, M. Farzan, B. Chen, H. Choe, Mechanisms of SARS-CoV-2 entry into cells, Nat. Rev. Mol. Cell Biol. 23 (2022), https://doi.org/10.1038/s41580-021-00418-x.
[4] J. Mercer, M. Schelhaas, A. Helenius, Virus entry by endocytosis, Annu. Rev. Biochem. 79 (2010), https://doi.org/10.1146/annurev-biochem-060208-104626.
[5] K. Knoops, M. Kikkert, S.H.E. Van Den Worm, J.C. Zevenhoven-Dobbe, Y. Van Der Meer, A.J. Koster, A.M. Mommaas, E.J. Snijder, SARS-coronavirus replication is supported by a reticulovesicular network of modified endoplasmic reticulum, PLoS Biol. 6 (2008), https://doi.org/10.1371/journal.pbio.0060226.
[6] G. Wolff, R.W.A.L. Limpens, J.C. Zevenhoven-Dobbe, U. Laugks, S. Zheng, A.W. M. de Jong, R.I. Koning, D.A. Agard, K. Grünewald, A.J. Koster, E.J. Snijder, M. Bárcena, A molecular pore spans the double membrane of the coronavirus replication organelle, Science 80 (2020) 369, https://doi.org/10.1126/SCIENCE.ABD3629.
[7] C.S. Goldsmith, K.M. Tatti, T.G. Ksiazek, P.E. Rollin, J.A. Comer, W.W. Lee, P. A. Rota, B. Bankamp, W.J. Bellini, S.R. Zaki, Ultrastructural characterization of SARS coronavirus, Emerg. Infect. Dis. 10 (2004), https://doi.org/10.3201/eid1002.030913.
[8] A. Aloor, R. Aradhya, P. Venugopal, B. Gopalakrishnan Nair, R. Suravajhala, Glycosylation in SARS-CoV-2 variants: a path to infection and recovery, Biochem. Pharmacol. 206 (2022), https://doi.org/10.1016/j.bcp.2022.115335.
[9] M. Hoffmann, H. Kleine-Weber, S. Schroeder, N. Krüger, T. Herrler, S. Erichsen, T.S. Schiergens, G. Herrler, N.H. Wu, A. Nitsche, M.A. Müller, C. Drosten, S. Pöhlmann, SARS-CoV-2 cell entry depends on ACE2 and TMPRSS2 and is blocked by a clinically proven protease inhibitor, Cell 181 (2020), https://doi.org/10.1016/j.cell.2020.02.052.
[10] A.Z. Mykytyn, T.I. Breugem, S. Riesebosch, D. Schipper, P.B. van den Doel, R. J. Rottier, M.M. Lamers, B.L. Haagmans, Sars-cov-2 entry into human airway organoids is serine protease-mediated and facilitated by the multibasic cleavage site, Elife 10 (2021), https://doi.org/10.7554/ELIFE.64508.
[11] A. Hegyi, J. Ziebuhr, Conservation of substrate specificities among coronavirus main proteases, J. Gen. Virol. 83 (2002), https://doi.org/10.1099/0022-1317-83-3-595.
[12] Y. Liu, C. Liang, L. Xin, X. Ren, L. Tian, X. Ju, H. Li, Y. Wang, Q. Zhao, H. Liu, W. Cao, X. Xie, D. Zhang, Y. Wang, Y. Jian, The development of Coronavirus 3C-Like protease (3CLpro) inhibitors from 2010 to 2020, Eur. J. Med. Chem. 206 (2020), https://doi.org/10.1016/j.ejmech.2020.112711.
[13] J. Lenard, A. Rabson, R. Vanderoef, Photodynamic inactivation of infectivity of human immunodeficiency virus and other enveloped viruses using hypericin and rose bengal: inhibition of fusion and syncytia formation, Proc. Natl. Acad. Sci. U. S.A. 90 (1993), https://doi.org/10.1073/pnas.90.1.158.
[14] X.Y. Pu, J.P. Liang, X.H. Xu, T. Wang, L.Y. Hua, R.F. Shang, Y. Liu, Y.M. Xing, Anti-influenza A virus effect of Hypericum perforatum L. extract, Virol. Sin. 24 (1) (2009) 19–27, https://doi.org/10.1007/s12250-009-2983-x.
[15] N. Nafee, A. Youssef, H. El-Gowelli, H. Asem, S. Kandil, Antibiotic-free nanotherapeutics: hypericin nanoparticles thereof for improved in vitro and in vivo antimicrobial photodynamic therapy and wound healing, Int. J. Pharm. 454 (2013), https://doi.org/10.1016/j.ijpharm.2013.06.067.
[16] P. Delcanale, F. Pennacchietti, G. Maestrini, B. Rodríguez-Amigo, P. Bianchini, A. Diaspro, A. Iagatti, B. Patrizi, P. Foggi, M. Agut, S. Nonell, S. Abbruzzetti, C. Viappiani, Subdiffraction localization of a nanostructured photosensitizer in bacterial cells, Sci. Rep. 5 (2015), https://doi.org/10.1038/srep15564.
[17] N. Choudhary, T.E. Collignon, D. Tewari, A. Bishayee, Hypericin and its anticancer effects: from mechanism of action to potential therapeutic application, Phytomedicine 105 (2022), https://doi.org/10.1016/j.phymed.2022.154356.

[18] X. Dong, Y. Zeng, Z. Zhang, J. Fu, L. You, Y. He, Y. Hao, Z. Gu, Z. Yu, C. Qu, X. Yin, J. Ni, L.J. Cruz, Hypericin-mediated photodynamic therapy for the treatment of cancer: A review, J. Pharm. Pharmacol. 73 (2021), https://doi.org/10.1093/jpp/rgaa018.

[19] R. Ritz, C. Scheidle, S. Noell, F. Roser, M. Schenk, K. Dietz, W.S.L. Strauss, In vitro comparison of hypericin and 5-aminolevulinic acid-derived protoporphyrin IX for photodynamic inactivation of medulloblastoma cells, PLoS One 7 (2012), https://doi.org/10.1371/journal.pone.0051974.

[20] Y. Zhang, H. Chen, M. Zou, R. Oerlemans, C. Shao, Y. Ren, R. Zhang, X. Huang, G. Li, Y. Cong, Hypericin inhibit alpha-coronavirus replication by targeting 3cl protease, Viruses 13 (2021), https://doi.org/10.3390/v13091825.

[21] A. da R. Matos, B.C. Caetano, J.L. de Almeida Filho, J.S.C. de C. Martins, M.G. P. de Oliveira, T. das C. Sousa, M.A.P. Horta, M.M. Siqueira, J.H. Fernandez, Identification of Hypericin as a Candidate Repurposed Therapeutic Agent for COVID-19 and Its Potential Anti-SARS-CoV-2 Activity, Front. Microbiol. 13 (2022), https://doi.org/10.3389/fmicb.2022.828984.

[22] P. Delcanale, E. Uriati, M. Mariangeli, A. Mussini, A. Moreno, D. Lelli, L. Cavanna, P. Bianchini, A. Diaspro, S. Abbruzzetti, C. Viappiani, The interaction of hypericin with SARS-CoV-2 reveals a multimodal antiviral activity, ACS Appl. Mater. Interfaces 14 (2022), https://doi.org/10.1021/acsami.1c22439.

[23] L.H. Bajrai, S.A. El-Kafrawy, A.M. Hassan, A.M. Tolah, R.S. Alnahas, S.S. Sohrab, M. Rehan, E.I. Azhar, In vitro screening of anti-viral and virucidal effects against SARS-CoV-2 by Hypericum perforatum and Echinacea, Sci. Rep. 12 (2022), https://doi.org/10.1038/s41598-022-26157-3.

[24] J. Joniova, M. Rebič, A. Strejčková, V. Huntosova, J. Staničová, D. Jancura, P. Miskovsky, G. Bánó, Formation of large hypericin aggregates in giant unilamellar vesicles—experiments and modeling, Biophys. J. 112 (2017) 966–975, https://doi.org/10.1016/j.bpj.2017.01.019.

[25] M. Van De Putte, T. Roskams, G. Bormans, A. Verbruggen, P.A.M. De Witte, The impact of aggregation on the biodistribution of hypericin, Int. J. Oncol. 28 (2006), https://doi.org/10.3892/ijo.28.3.655.

[26] X. Liu, C. Jiang, Y. Li, W. Liu, N. Yao, M. Gao, Y. Ji, D. Huang, Z. Yin, Z. Sun, Y. Ni, J. Zhang, Evaluation of hypericin: effect of aggregation on targeting biodistribution, J. Pharm. Sci. 104 (2015), https://doi.org/10.1002/jps.24230.

[27] V. Huntosova, Z. Nadova, L. Dzurova, V. Jakusova, F. Sureau, P. Miskovsky, Cell death response of U87 glioma cells on hypericin photoactivation is mediated by dynamics of hypericin subcellular distribution and its aggregation in cellular organelles, Photochem. Photobiol. Sci. 11 (2012) 1428–1436, https://doi.org/10.1039/c2 pp05409d.

[28] V. Huntošová, S. Datta, L. Lenkavská, M. MáčAjová, B. Bilčík, B. Kundeková, I. Čavarga, J. Kronek, A. Jutková, P. Miškovský, D. Jancura, Alkyl chain length in poly(2-oxazoline)-based amphiphilic gradient copolymers regulates the delivery of hydrophobic molecules: a case of the biodistribution and the photodynamic activity of the photosensitizer hypericin, Biomacromolecules 22 (2021), https://doi.org/10.1021/acs.biomac.1c00768.

[29] M. Olivo, C.Y. Fu, V. Raghavan, W.K.O. Lau, New frontier in hypericin-mediated diagnosis of cancer with current optical technologies, Ann. Biomed. Eng. 40 (2012), https://doi.org/10.1007/s10439-011-0462-7.

[30] B. Taşkonak, G. Aylaz, M. Andac, E. Güven, B. Ozkahraman, I. Perçin, A. Kılıç Süloğlu, Hypericin-loaded chitosan nanoparticles for enhanced photodynamic therapy in A549 lung cancer cells, BioNanoScience 13 (2) (2023) 352–364, https://doi.org/10.1007/s12668-023-01099-w.

[31] V. Pevná, L. Zauška, A. Benziane, G. Vámosi, V. Girman, M. Miklóšová, V. Zeleňák, V. Huntošová, M. Almáši, Effective transport of aggregated hypericin encapsulated in SBA-15 nanoporous silica particles for photodynamic therapy of cancer cells, J. Photochem. Photobiol. B Biol. 247 (2023), https://doi.org/10.1016/j.jphotobiol.2023.112785.

[32] P. Agostinis, A. Vantieghem, W. Merlevede, P.A.M. De Witte, Hypericin in cancer treatment: more light on the way, Int. J. Biochem. Cell Biol. 34 (2002) 221–241, https://doi.org/10.1016/S1357-2725(01)00126-1.

[33] J.M. Farrell, C.Y. Zhao, K.M. Tarquinio, S.P. Brown, Causes and consequences of COVID-19-associated bacterial infections, Front. Microbiol. 12 (2021), https://doi.org/10.3389/fmicb.2021.682571.

[34] M.A. Hendaus, F.A. Jomha, Covid-19 induced superimposed bacterial infection, J. Biomol. Struct. Dyn. 39 (2021), https://doi.org/10.1080/07391102.2020.1772110.

[35] E. Moreno-García, P. Puerta-Alcalde, L. Letona, F. Meira, G. Dueñas, M. Chumbita, N. Garcia-Pouton, P. Monzó, C. Lopera, L. Serra, C. Cardozo, M. Hernandez-Meneses, V. Rico, M. Bodro, L. Morata, M. Fernandez-Pittol, I. Grafia, P. Castro, J. Mensa, J.A. Martínez, G. Sanjuan, M.A. Marcos, A. Soriano, C. Garcia-Vidal, Bacterial co-infection at hospital admission in patients with COVID-19: Bacterial co-infections in COVID-19, Int. J. Infect. Dis. 118 (2022), https://doi.org/10.1016/j.ijid.2022.03.003.

[36] L.D. Dias, K.C. Blanco, V.S. Bagnato, COVID-19: beyond the virus. The use of photodynamic therapy for the treatment of infections in the respiratory tract, Photodiagnosis Photodyn. Ther. 31 (2020) 101804, https://doi.org/10.1016/j.pdpdt.2020.101804.

[37] E. Beňová, V. Hornebecq, V. Zeleňák, V. Huntošová, M. Almáši, M. Máčajová, D. Bergé-Lefranc, pH-responsive mesoporous silica drug delivery system, its biocompatibility and co-adsorption/co-release of 5-Fluorouracil and Naproxen, Appl. Surf. Sci. 561 (2021), https://doi.org/10.1016/j.apsusc.2021.150011.

[38] Y. Sun, L. Zheng, Y. Yang, X. Qian, T. Fu, X. Li, Z. Yang, H. Yan, C. Cui, W. Tan, Metal–Organic Framework Nanocarriers for Drug Delivery in Biomedical Applications, Nano-Micro Lett. 12 (2020), https://doi.org/10.1007/s40820-020-00423-3.

[39] M. Almáši, A review on state of art and perspectives of Metal-Organic frameworks (MOFs) in the fight against coronavirus SARS-CoV-2, J. Coord. Chem. 74 (2021), https://doi.org/10.1080/00958972.2021.1965130.

[40] J.L. Obeso, M.T. Huxley, C. Leyva, J.G. Flores, N. Martín-Guaregua, M. Viniegra, J. Aguilar-Pliego, J.A. los Reyes Ibarra, R.A. Peralta, The role of dynamic metal-ligand bonds in metal-organic framework chemistry, Coord. Chem. Rev. 496 (2023) 215403, https://doi.org/10.1016/j.ccr.2023.215403.

[41] Z. Lin, D. Liao, C. Jiang, A. Nezamzadeh-Ejhieh, M. Zheng, H. Yuan, J. Liu, H. Song, C. Lu, Current status and prospects of MIL-based MOF materials for biomedicine applications, RSC Med. Chem. 14 (2023), https://doi.org/10.1039/d3md00397c.

[42] M. Zou, M. Dong, T. Zhao, Advances in Metal-Organic Frameworks MIL-101(Cr), Int. J. Mol. Sci. 23 (2022), https://doi.org/10.3390/ijms23169396.

[43] O.I. Lebedev, F. Millange, C. Serre, G. Van Tendeloo, G. Férey, First direct imaging of giant pores of the metal-organic framework MIL-101, Chem. Mater. 17 (2005), https://doi.org/10.1021/cm051870o.

[44] M.Y. Zorainy, M. Gar Alalm, S. Kaliaguine, D.C. Boffito, Revisiting the MIL-101 metal-organic framework: design, synthesis, modifications, advances, and recent applications, J. Mater. Chem. A 9 (2021), https://doi.org/10.1039/d1ta06238g.

[45] M. Beiranvand, G. Dehghan, An analytical review of the therapeutic application of recent trends in MIL-based delivery systems in cancer therapy, Microchim. Acta 192 (2025) 89, https://doi.org/10.1007/s00604-024-06944-7.

[46] S.E. Miller, M.H. Teplensky, P.Z. Moghadam, D. Fairen-Jimenez, Metal-organic frameworks as biosensors for luminescence-based detection and imaging, Interface Focus 6 (2016), https://doi.org/10.1098/rsfs.2016.0027.

[47] Y. Li, W.X. Wang, Internalization of the metal-organic framework MIL-101(Cr)-NH2 by a freshwater alga and transfer to zooplankton, Environ. Sci. Technol. 57 (2023), https://doi.org/10.1021/acs.est.2c03780.

[48] J. Shang, Y. Chen, F. Wang, J. Yang, Y. Li, L. Yang, X. Liu, Z. Zhong, C. Yue, M. Zhou, A Multifunctional MIL-101-NH(2)(Fe) nanoplatform for synergistic melanoma therapy, Int. J. Nanomed. 20 (2025) 969–988, https://doi.org/10.2147/IJN.S502089.

[49] A. Rajan, C. Yazhini, M.D. Dhileepan, B. Neppolian, Leveraging the photocatalytic Cr (VI) reduction by an IRMOF-3@NH2-MIL-101 (Fe) heterostructure based on interfacial Lewis acid-base interaction, Chemosphere 352 (2024), https://doi.org/10.1016/j.chemosphere.2024.141473.

[50] X.Y. Xu, B. Yan, An efficient and sensitive fluorescent pH sensor based on amino functional metal-organic frameworks in aqueous environment, Dalt. Trans. 45 (2016), https://doi.org/10.1039/c6dt00361c.

[51] Y. Wang, Z. Wang, P. Gupta, J.J. Morrissey, R.R. Naik, S. Singamaneni, Enhancing the stability of COVID-19 serological assay through metal–organic framework encapsulation, Adv. Healthc. Mater. 10 (2021), https://doi.org/10.1002/adhm.202100410.

[52] A. Elgazar, R. Sabouni, M. Ghommem, A.F. Majdalawieh, Novel metal–organic framework biosensing platform for detection of COVID-19 RNA, Sci. Rep. 14 (2024) 25437, https://doi.org/10.1038/s41598-024-75668-8.

[53] A. Elgazar, R. Sabouni, M. Ghommem, A.F. Majdalawieh, Sustainable synthesis of MOF for COVID-19 detection using a 23 factorial design, Colloids Surf. A Physicochem. Eng. Asp. 705 (2025) 135616, https://doi.org/10.1016/j.colsurfa.2024.135616.

[54] X. Wang, G. Clavier, Y. Zhang, K. Batra, N. Xiao, G. Maurin, B. Ding, A. Tissot, C. Serre, A MOF/DNA luminescent sensing platform for detection of potential COVID-19 biomarkers and drugs, Chem. Sci. 14 (2023), https://doi.org/10.1039/d3sc00106g.

[55] X. Wang, K. Batra, G. Clavier, G. Maurin, B. Ding, A. Tissot, C. Serre, Ln-MOF based ratiometric luminescent sensor for the detection of potential COVID-19 drugs, Chem. - A Eur. J. 29 (2023), https://doi.org/10.1002/chem.202203136.

[56] A.V. Desai, S.M. Vornholt, L.L. Major, R. Ettlinger, C. Jansen, D.N. Rainer, R. de Rome, V. So, P.S. Wheatley, A.K. Edward, C.G. Elliott, A. Pramanik, A. Karmakar, A.R. Armstrong, C. Janiak, T.K. Smith, R.E. Morris, Surface-functionalized metal-organic frameworks for binding coronavirus proteins, ACS Appl. Mater. Interfaces (2023), https://doi.org/10.1021/acsami.2c21187.

[57] M. Dahri, M.M. Sadeghi, S.S. Abolmaali, A computational study of metal–organic frameworks (MOFs) as potential nanostructures to combat SARS-CoV-2, Sci. Rep. 12 (2022), https://doi.org/10.1038/s41598-022-19845-7.

[58] O.E. Plastiras, P. Bouquet, C. Lecœur, J. Dhainaut, J.P. Dacquin, S. Royer, T. Loiseau, A. Goffard, C. Volkringer, Cytotoxicity and effectiveness of archetypal Metal-Organic Frameworks (HKUST-1, UiO-66, MIL-53, MIL-125) against coronaviruses (HCoV-229E and SARS-CoV-2), Microporous Mesoporous Mater. 367 (2024), https://doi.org/10.1016/j.micromeso.2023.112975.

[59] A. Chołuj, N.I. Nikishkin, M.J. Chmielewski, Facile post-synthetic deamination of MOFs and the synthesis of the missing parent compound of the MIL-101 family, Chem. Commun. 53 (2017), https://doi.org/10.1039/c7cc06054h.

[60] G. Zelenková, T. Zelenka, M. Almáši, Characterizing mesoporosity in MOFs: a thermoporometry approach, J. Therm. Anal. Calorim. 149 (2024) 12675–12683, https://doi.org/10.1007/s10973-024-13667-7.

[61] T. Zelenka, K. Simanova, R. Saini, G. Zelenkova, S.P. Nehra, A. Sharma, M. Almasi, Carbon dioxide and hydrogen adsorption study on surface-modified HKUST-1 with diamine/triamine, Sci. Rep. 12 (2022), https://doi.org/10.1038/s41598-022-22273-2.

[62] C. Huang, M.F. Becker, J.W. Keto, D. Kovar, Schneider, C. A., Rasband, W. S., & Eliceiri, K. W. (2012). NIH Image to ImageJ: 25 years of image analysis. Nature Methods, 9(7), 671–675. doi: 10.1038/nmeth.2089, J. Appl. Phys. 102 (2012).

[63] M. Almáši, V. Zeleňák, P. Palotai, E. Beňová, A. Zeleňáková, Metal-organic framework MIL-101(Fe)-NH2 functionalized with different long-chain

polyamines as drug delivery system, Inorg. Chem. Commun. 93 (2018), https://doi.org/10.1016/j.inoche.2018.05.007.
[64] O. Ivashchenko, Ł. Przysiecka, B. Peplińska, D. Flak, E. Coy, M. Jarek, T. Zalewski, A. Musiał, S. Jurga, Organic-inorganic hybrid nanoparticles synthesized with hypericum perforatum extract: potential agents for photodynamic therapy at ultra-low power light, ACS Sustain. Chem. Eng. 9 (2021), https://doi.org/10.1021/acssuschemeng.0c07036.
[65] K. Roztocki, M. Rauche, V. Bon, S. Kaskel, E. Brunner, D. Matoga, Combining in situ techniques (XRD, IR, and 13C NMR) and gas adsorption measurements reveals CO2-induced structural transitions and high CO2/CH4 selectivity for a flexible metal-organic framework JUK-8, ACS Appl. Mater. Interfaces 13 (2021), https://doi.org/10.1021/acsami.1c07268.
[66] L. Zauška, D. Volavka, M. Lisnichuk, T. Zelenka, E. Kinnertová, G. Zelenková, J. Bednarčík, V. Zeleňák, A. Sharma, S. Pal Nehra, A. Eštoková, M. Almáši, Tuning the photocatalytic performance of mesoporous silica-titanium dioxide and cobalt titanate for methylene blue and Congo red adsorption/photodegradation: Impact of azo dyes concentration, catalyst mass, wavelength, reusability and kinetic properties, J. Photochem. Photobiol. A Chem. 451 (2024), https://doi.org/10.1016/j.jphotochem.2024.115522.
[67] M. Thommes, K. Kaneko, A.V. Neimark, J.P. Olivier, F. Rodriguez-Reinoso, J. Rouquerol, K.S.W. Sing, Physisorption of gases, with special reference to the evaluation of surface area and pore size distribution (IUPAC Technical Report), Pure Appl. Chem. 87 (2015), https://doi.org/10.1515/pac-2014-1117.
[68] L. Zauska, E. Benova, M. Urbanová, J. Brus, V. Zelenak, V. Hornebecq, M. Almáši, Adsorption and release properties of drug delivery system naproxen-SBA-15 : effect of surface polarity , sodium / acid drug form and pH, J. Funct. Biomater. 13 (2022) 275, https://doi.org/10.3390/jfb13040275.
[69] M. Almáši, N. Király, V. Zeleňák, M. Vilková, S. Bourrelly, Zinc(ii) and cadmium (ii) amorphous metal-organic frameworks (aMOFs): Study of activation process and high-pressure adsorption of greenhouse gases, RSC Adv. 11 (2021), https://doi.org/10.1039/d1ra02938j.
[70] Ľ. Zauška, P. Pillárová, D. Volavka, E. Kinnertová, J. Bednarčík, J. Brus, V. Hornebecq, M. Almáši, Kinetic adsorption mechanism of cobalt(II) ions and Congo red on pristine and Schiff base-surface-modified MIL-101(Fe)-NH2, Microporous Mesoporous Mater. 386 (2025) 113493, https://doi.org/10.1016/j.micromeso.2025.113493.
[71] A. Benziane, V. Huntošová, V. Pevná, L. Zauška, G. Vámosi, A. Hovan, G. Zelenková, V. Zeleňák, M. Almáši, Synergistic effect of folic acid and hypericin administration to improve the efficacy of photodynamic therapy via folate receptors, J. Photochem. Photobiol. B Biol. 261 (2024) 113046, https://doi.org/10.1016/j.jphotobiol.2024.113046.
[72] V. Huntosova, L. Alvarez, L. Bryndzova, Z. Nadova, D. Jancura, L. Buriankova, S. Bonneau, D. Brault, P. Miskovsky, F. Sureau, Interaction dynamics of hypericin with low-density lipoproteins and U87-MG cells, Int. J. Pharm. 389 (2010) 32–40, https://doi.org/10.1016/j.ijpharm.2010.01.010.
[73] C. Lin, Z. Zou, Z. Lei, L. Wang, Y. Song, Fluorescent metal-organic frameworks MIL-101(Al)-NH2 for rapid and sensitive detection of ellagic acid, Spectrochim. Acta - Part A Mol. Biomol. Spectrosc. 242 (2020), https://doi.org/10.1016/j.saa.2020.118739.
[74] M. Barroso, M.G. Monaghan, R. Niesner, R.I. Dmitriev, Probing organoid metabolism using fluorescence lifetime imaging microscopy (FLIM): The next frontier of drug discovery and disease understanding, Adv. Drug Deliv. Rev. 201 (2023), https://doi.org/10.1016/j.addr.2023.115081.
[75] D. Ribatti, The chick embryo chorioallantoic membrane (CAM). A multifaceted experimental model, Mech. Dev. 141 (2016), https://doi.org/10.1016/j.mod.2016.05.003.
[76] V. Huntosova, S. Gay, P. Nowak-Sliwinska, S.K. Rajendran, M. Zellweger, H. Van Den Bergh, G. Wagnières, In vivo measurement of tissue oxygenation by time-resolved luminescence spectroscopy: Advantageous properties of dichlorotris(1, 10-phenanthroline)- ruthenium(II) hydrate, J. Biomed. Opt. 19 (2014), https://doi.org/10.1117/1.JBO.19.7.077004.
[77] P. Nowak-Sliwinska, T. Segura, M.L. Iruela-Arispe, The chicken chorioallantoic membrane model in biology, medicine and bioengineering, Angiogenesis 17 (2014), https://doi.org/10.1007/s10456-014-9440-7.
[78] H. Kimura, M.S. Harris, T. Sakamoto, R. Gopalakrishna, U. Gundimeda, J.Z. Cui, C. Spee, D.R. Hinton, S.J. Ryan, Hypericin inhibits choroidal endothelial cell proliferation and cord formation in vitro, Curr. Eye Res. 16 (1997), https://doi.org/10.1076/ceyr.16.10.967.9019.
[79] W. Zhang, R.E. Lawa, D.R. Hintona, Y. Su, W.T. Couldwell, Growth inhibition and apoptosis in human neuroblastoma SK-N-SH cells induced by hypericin, a potent inhibitor of protein kinase C, Cancer Lett. 96 (1995) 31–35, https://doi.org/10.1016/0304-3835(95)03914-I.
[80] I. Takahashi, S. Nakanishi, E. Kobayashi, H. Nakano, K. Suzuki, T. Tamaoki, Hypericin and pseudohypericin specifically inhibit protein kinase C: Possible relation to their antiretroviral activity, Biochem. Biophys. Res. Commun. 165 (1989), https://doi.org/10.1016/0006-291X(89)92730-7.
[81] G. Lavie, M. Mandel, S. Hazan, T. Barliya, M. Blank, A. Grunbaum, D. Meruelo, A. Solomon, Anti-angiogenic activities of hypericin in vivo: Potential for ophthalmologic applications, Angiogenesis 8 (2005), https://doi.org/10.1007/s10456-005-3828-3.
[82] B. Martínez-Poveda, A.R. Quesada, M.Á. Medina, Hypericin in the dark inhibits key steps of angiogenesis in vitro, Eur. J. Pharmacol. 516 (2005), https://doi.org/10.1016/j.ejphar.2005.03.047.
[83] K. Siposova, V. Huntosova, D. Sedlakova, M. Macajova, B. Bilcik, A.V. Nair, S. Nair, V. Hovhannisyan, S.J. Chen, A. Musatov, Biocompatible zeolite-dye composites with anti-amyloidogenic properties, Int. J. Biol. Macromol. 251 (2023) 126331, https://doi.org/10.1016/j.ijbiomac.2023.126331.
[84] Y. Liu, T. Jiang, Z. Liu, Metal-organic frameworks for bioimaging: strategies and challenges, Nanotheranostics 6 (2022), https://doi.org/10.7150/ntno.63458.
[85] P.M. Stanley, C. Thomas, E. Thyrhaug, A. Urstoeger, M. Schuster, J. Hauer, B. Rieger, J. Warnan, R.A. Fischer, Entrapped molecular photocatalyst and photosensitizer in metal-organic framework nanoreactors for enhanced solar CO2Reduction, ACS Catal. 11 (2021), https://doi.org/10.1021/acscatal.0c04673.
[86] W. Zhang, K. Wei, W. Huang, J. Yang, Y. Gan, S. Zhang, A joint mechanism for singlet oxygen generation by diketone-anchored MIL-101: Exciton-mediated energy transfer and photosensitization, Appl. Catal. A Gen. 626 (2021), https://doi.org/10.1016/j.apcata.2021.118360.
[87] L. Cui, X. Wang, Z. Liu, Z. Li, Z. Bai, K. Lin, J. Yang, Y. Cui, F. Tian, Metal-organic framework decorated with glycyrrhetinic acid conjugated chitosan as a pH-responsive nanocarrier for targeted drug delivery, Int. J. Biol. Macromol. 240 (2023), https://doi.org/10.1016/j.ijbiomac.2023.124370.
[88] E. Linnane, S. Haddad, F. Melle, Z. Mei, D. Fairen-Jimenez, The uptake of metal-organic frameworks: a journey into the cell, Chem. Soc. Rev. 51 (2022), https://doi.org/10.1039/d0cs01414a.
[89] S. Wang, F. Guo, K. Liu, H. Wang, S. Rao, P. Yang, C. Jiang, Endocytosis of the receptor-binding domain of SARS-CoV spike protein together with virus receptor ACE2, Virus Res. 136 (2008), https://doi.org/10.1016/j.virusres.2008.03.004.
[90] E. Vanhulle, J. Stroobants, B. Provinciael, A. Camps, S. Noppen, P. Maes, K. Vermeire, SARS-CoV-2 Permissive glioblastoma cell line for high throughput antiviral screening, Antiviral Res. 203 (2022), https://doi.org/10.1016/j.antiviral.2022.105342.
[91] V. Pevná, Ľ. Zauška, M. Almáši, A. Hovan, G. Bánó, M. Máčajová, B. Bilčík, V. Zeleňák, V. Huntošová, Redistribution of hydrophobic hypericin from nanoporous particles of SBA-15 silica in vitro, in cells and in vivo, Int. J. Pharm. 643 (2023), https://doi.org/10.1016/j.ijpharm.2023.123288.
[92] Y. Zhang, C. Sun, Y. Ji, K. Bi, H. Tian, B. Wang, Engineering linker-defects of MIL-101 series metal organic frameworks for boosted Yb(III) adsorption, Sep. Purif. Technol. 330 (2024), https://doi.org/10.1016/j.seppur.2023.125293.
[93] Y. Luo, R. Su, Preparation of NH2-MIL-101(Fe) Metal Organic Framework and Its Performance in Adsorbing and Removing Tetracycline, Int. J. Mol. Sci. 25 (2024), https://doi.org/10.3390/ijms25189855.
[94] R. Chang, J. Ma, J. Wang, Y. Liu, X. Guo, H. Qu, Efficient adsorption of dyes using polyethyleneimine-modified NH2-MIL-101(Al) and its sustainable application as a flame retardant for an epoxy resin, ACS Omega 5 (2020), https://doi.org/10.1021/acsomega.0c04118.
[95] P. Mukherjee, R. Adhikary, M. Halder, J.W. Petrich, P. Miskovsky, Accumulation and interaction of hypericin in low-density lipoprotein - a photophysical study, Photochem. Photobiol. 84 (2008), https://doi.org/10.1111/j.1751-1097.2007.00234.x.
[96] L. Blascakova, D. Horvath, D. Belej, G. Wagnieres, P. Miskovsky, D. Jancura, V. Huntosova, Hypericin can cross barriers in the chicken's chorioallantoic membrane model when delivered in low-density lipoproteins, Photodiagnosis Photodyn. Ther. 23 (2018) 306–313, https://doi.org/10.1016/j.pdpdt.2018.07.009.
[97] J. Hritz, S. Kascakova, J. Ulicny, P. Miskovsky, Influence of structure of human, rat, and bovine serum albumins on binding properties of photoactive drug hypericin, Biopolym. - Biospectroscopy Sect., (2002), https://doi.org/10.1002/bip.10110.
[98] B.J. Langford, M. So, S. Raybardhan, V. Leung, D. Westwood, D.R. MacFadden, J. P.R. Soucy, N. Daneman, Bacterial co-infection and secondary infection in patients with COVID-19: a living rapid review and meta-analysis, Clin. Microbiol. Infect. 26 (2020), https://doi.org/10.1016/j.cmi.2020.07.016.
[99] B. Kaçmaz, Ş. Keske, U. Sişman, S.T. Ateş, M. Güldan, Y. Beşli, E. Palaoğlu, N. Çakar, Ö. Ergönül, COVID-19 associated bacterial infections in intensive care unit: a case control study, Sci. Rep. 13 (2023), https://doi.org/10.1038/s41598-023-39632-2.
[100] G. Wu, J. Lu, D. Liu, Y. He, Characteristics and risk factors of secondary bacterial infections in COVID-19 patients, Antimicrob. Steward. Healthc. Epidemiol. 3 (2023), https://doi.org/10.1017/ash.2023.425.
[101] B.A. Thomas-Moore, C.A. del Valle, R.A. Field, M.J. Marín, Recent advances in nanoparticle-based targeting tactics for antibacterial photodynamic therapy, Photochem. Photobiol. Sci. 21 (2022) 1111–1131, https://doi.org/10.1007/s43630-022-00194-3.
[102] P. Dharmaratne, D.N. Sapugahawatte, B. Wang, C.L. Chan, K.M. Lau, C. Lau, K. P. Fung, D.K. Ng, M. Ip, Contemporary approaches and future perspectives of antibacterial photodynamic therapy (aPDT) against methicillin-resistant Staphylococcus aureus (MRSA): a systematic review, Eur. J. Med. Chem. 200 (2020) 112341, https://doi.org/10.1016/j.ejmech.2020.112341.
[103] S. Sethi, V. Rathod, Isolation and chemical immobilization of -specific bacteriophage with NH2-MIL-101(Fe) MOF, a high photoluminescence rod-shaped microcrystals for low-level bacteria detection, Appl. Organomet. Chem. 38 (2024) e7624.
[104] J. Liu, W. Cheng, K. Zhang, H. Liu, J. Li, J. Tressel, S. Chen, High-efficiency photodynamic antibacterial activity of NH2-MIL-101(Fe)@MoS2/ZnO ternary composites, ACS Appl. Bio Mater. 5 (2022), https://doi.org/10.1021/acsabm.2c00439.
[105] N. Li, Z. He, J. Gan, X. Qi, S. Bian, Y. Chen, B. Liu, H. Lai, T. Jin, Disinfection of bacteria and viruses under near infrared light by tunable self-assembled nanomaterial NH2-MIL-101-xAu based on photothermal and photodynamic mechanisms, J. Environ. Chem. Eng. 12 (2024) 114114, https://doi.org/10.1016/j.jece:2024.114114.